Development of High-Performance Gas-Coupled Ultrasonic Transducers for Inspection of Unpiggable Natural Gas Pipelines

Public Final Report

Contract Number: DTPH5616T00003

Reporting Period: Final Report, September 30, 2016 – September 29, 2019

Date of Report: February 7, 2020

Prepared for:
U.S. Department of Transportation
Pipeline and Hazardous Materials Safety Administration

Prepared by:
Vincent Fratello
Principal Investigator and Project Manager
Director of Materials Research
Quest Integrated, LLC
v.fratello@qi2.com
(253) 480-2027

Phil Bondurant, Vice President of Engineering, Quest Integrated, LLC
Ali Minachi, Director of Ultrasonics, Quest Integrated, LLC

For contract period ending: September 29, 2019

Quest Integrated, LLC (Qi2)
19823 58th Place S, Suite 200
Kent, Washington 98032
(253) 872-9500
www.qi2.com

Objective

New dry-coupled ultrasonic transducer (UT) techniques were investigated to determine feasibility for in-line inspection (ILI) of unpiggable gas pipelines, especially for wall loss measurements, but also for internal geometry/caliper tools. This novel technology will produce more accurate, higher-temperature resistant UT probes and have additional uses in inspection for wall loss and cracks in liquid pipelines. Accurate wall thickness data can be fed into API 579 Fitness for Service (FFS) analysis, or failure criteria such as ASME B31G or RSTRENG to allow calculation of remaining wall strength. A 90% probability of detection was initially targeted at 800 psi, but more stringent criteria of thickness measurement down to 6 mm wall thickness at 250 psi have been applied to assure use in distribution lines. These tools will contribute to assessment of pipeline integrity/risks and materials evaluation.

Executive Summary

An estimated $7 billion is spent each year on system inspections, testing, maintenance and repair in gas pipelines. Inspection of unpiggable gas pipelines for thickness and crack detection is substantially an unanswered challenge for gas transmission companies. The most commonly used method for inspection and corrosion mapping in *piggable* gas transmission pipelines is Magnetic Flux Leakage (MFL). However, MFL tools typically cannot be used effectively in unpiggable pipelines because of obstructions and lack of launcher/receiver facilities. MFL also has limitations in accuracy and can't provide precise thickness measurement, requiring the verification of most indications by other methods. MFL tools have difficulty detecting corrosion at certain orientations/locations in pipes and over large areas. Additionally, the large and heavy MFL magnets require a large pressure differential to push them through pipelines resulting in a greater chance of getting stuck in a pipeline, especially in unpiggable pipelines with features such as sharp turns, valves, reducers and other obstructions. Therefore, unpiggable pipelines are currently typically inspected by hydrotesting or excavation and direct inspection.

Ultrasonic transducer (UT) in-line inspection (ILI) tools have the advantage of making accurate corrosion measurements and are less likely to be trapped because a standoff from the pipe wall is possible. UT ILI tools are commercially available for use in *liquid* pipelines for wall thickness measurement and crack detection. However, in gas pipelines the impedance matching of acoustic signals to gas at both interfaces is poor with a 130,000:1 impedance difference between gas and steel at 1 bar (14.7 psi) and ~7,000:1 at a low end distribution line pressure of 250 psi. Transmitting ultrasound from a solid to a gas and back is like trying to put light through a mirror. The majority of the intensity is reflected at each interface, especially interfaces between the pipe and the gas, which are not subject to impedance matching coatings. Without a liquid couplant, it is difficult to impossible to receive a measurable signal from the back wall of the pipe. If issues of signal strength and sensitivity could be overcome, dry-coupled UT with reasonable gas pressures would have advantages of accuracy and ability to navigate unpiggable pipes.

In this project, Quest Integrated, LLC (Qi2) has undertaken to put together a set of technologies to enable gas-coupled UT inspection of gas pipelines. No single innovation can make this possible, but the following have been used collectively to achieve the goals.

1. ***Improvement of piezoelectric materials****.*

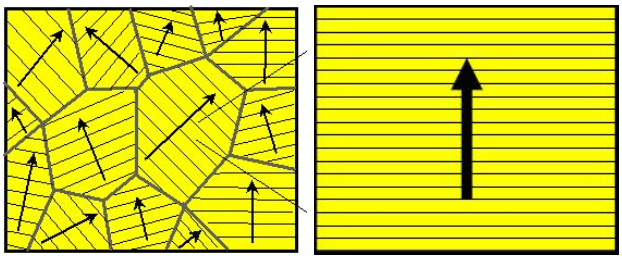

Figure 1: Piezoelectric ceramics (left) are omni-directional and incoherent like a light emitting diode. Single crystals (right) are directional and coherent similar to a laser.

Current ILI tools use piezoelectric elements that are sometimes referred to as crystals, but are actually ceramics that contain crystallite grains of many different orientations that produce ultrasonic pulses that are omnidirectional and incoherent. Single crystals have inherent advantages over ceramic materials (Figure 1) in transducer efficiency because of improved coherency, directionality and coupling. Innovative single crystals of lead zirconate titanate (PZT) were previously technologically unfeasible, but have been developed under this project. Single crystal transducer prototypes have shown an efficiency improvement of a factor of three over ceramics on both send and receive, resulting in approximately an order of magnitude increase in system sensitivity. The development of these crystals has been completed and is ready to proceed to higher volumes.

2. Improved Transducer Designs

Qi2 has taken the state of the art in transducer designs and modeled it by two different methods. The transducers have been improved in all aspects. This adds efficiency to the output and detection capabilities of the transducer, producing higher intensity and better separated reflected signals.

3. Improved Electronics

The largest volume elements in the ILI tool design are the electronics and batteries. Reduced power consumption is critical. With this in mind, the electronics for pulse generation, detection and signal analysis have been analyzed, modeled and improved to be more efficient. Moreover, Qi2 has been working on miniaturization of these electronics to permit a much shorter tool with much of the data analysis on board to reduce storage requirements.

These combined design improvements have now shown the feasibility of gas-coupled ultrasonic transduction (GCUT) wall thickness measurement and internal geometry in a gas pipeline with no liquid couplant and gas pressures within the operating range of most existing pipelines. Prototypes have determined the thickness of a 6 mm steel plate to within $\pm$0.05 mm at a standoff of 25 mm and a gas pressure of 250 psi. This method should be capable of determining absolute wall loss as is not currently possible. This new technology can advance industry standards for protection of people, property and the environment. All milestones of this project were completed. In the next phase these designs will be commercialized in an ILI tool.

Requirements

A meeting with the Gas Technology Institute (GTI) occurred on December 7, 2016 to support requirements development, advice for corrosion features, and report review. GTI agreed that the

overall tool specifications would mirror the requirements from the Electromagnetic Acoustic Transducer (EMAT) ILI tools currently under development at Qi2. GTI provided information regarding typical corrosion size and depth distributions. The flaw requirements were combined with the tool geometry requirements and environmental requirements to complete the overall tool requirements. The resulting document was approved by GTI.

The B31G standard provides procedures for evaluating metal loss in pressurized pipelines and piping systems. Level 0 and 1 evaluation procedures require, as an input, the maximum depth of the corroded area, d, and the longitudinal extent of the corroded area, L. The Level 2 procedure uses the effective area method. In this case, either a grid pattern of remaining wall thickness measurements is taken, or, as an alternative, multiple wall thickness measurements can be taken along a "river bottom" path through the deepest areas of metal loss.

The target requirements are reflected in Table I.

Table I: Single crystal UT tool target requirements

Direct Requirements	***Low Flow***
Product temperature range	40F - 90F (4.4 - 32.2 C)
Product flow rate	Not Applicable
Product operating pressure	Up to 1,000 psig (6,894,757 Pa)
Acceptable axial tool speed range	<1 foot/sec (30.5 cm/sec)
Maximum inspection length	A function of the locomotive platform
Typical wall thickness	0.375" (9.5 mm)
Maximum wall thickness	0.500" (12.7 mm)
Minimum wall thickness	0.25" (6.4 mm)
Pipeline diameter range	6" – 16" (15.2 – 40.6 cm); Initial target: 8" (20.3 cm)
Multiple wall thicknesses in a single inspection run	Not typical
Collapse Factor/ID clearance (percent of OD) to account for unpiggable features	85% or better
Minimum bend radius	1.5xD
Bi-directionality	Yes
Crack/Metal loss/Pipe feature discrimination (POI)	Yes
Wall thickness measurement (derived requirement)	Yes
Coatings	CTE, FBE, Wax, Tapes and Wraps
Locomotion	Tethered/Crawler
Sensor foot print	0.25" (diameter or square)
Longitudinal (axial) sample spacing	<0.25"
Circumferential sample spacing	<0.25"
Sensor depth resolution	0.005"

Notes:

(1) ***Pressure***: Most pressures will be less than 500 psig for the LDC transmission sector, however

there are a limited number of instances with higher pressures. It has not been determined whether a minimum pressure is required for operation.

(2) ***Unpiggable features and diameter***: A survey of OTD sponsors provided the pipe size ranges in Figure 2. Many of these lines have unpiggable features like non-full-bore valves, diameter changes, large inner weld beads, etc. This is why a large (better than 85%) collapsibility feature was selected. The mechanical clearance is a function of the distance needed (closer is better) to get the tool/sensor close to the wall, but also to keep wear minimized. Since gas pipe is outer diameter controlled and thickness can vary, as well as bend radius for appurtenances, the clearance range should account for these variations.

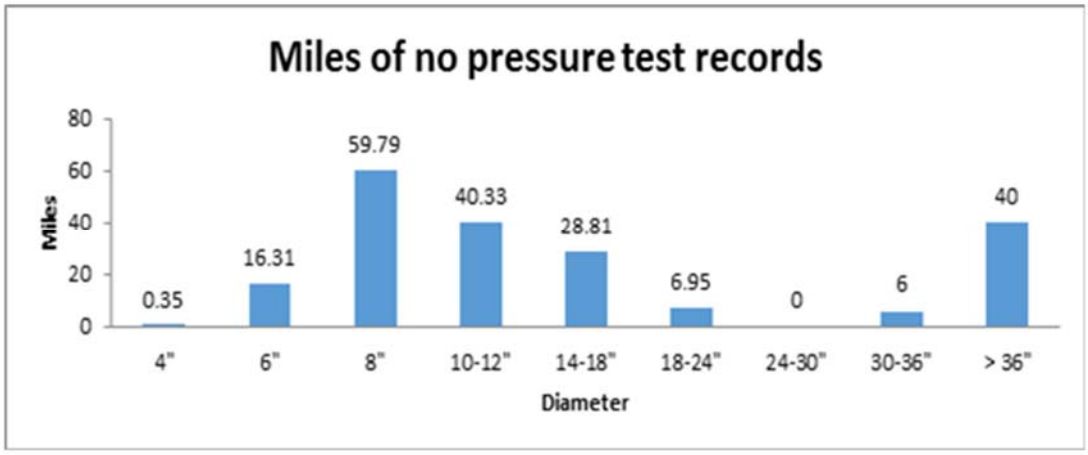

Figure 2: Distribution of miles with no pressure test records versus pipe diameter.

The 3x thickness (3t) criterion for interacting flaws in a 0.25”-thick wall is 0.75” (19 mm), so the sensor footprint and sampling density needs to be sufficient to provide data necessary to make the interacting flaw decision. Clearly an ultrasonic transducer/sensor (UT) that has a 0.75” or larger sensing footprint would make the “interacting” determination more difficult. The other B31G criterion is to measure the deepest flaw over the corroded area. This requires the smallest footprint sensor possible so that it maximizes the amplitude of the reflected sound energy at the bottom of a corrosion pit. Our final target sensing footprint for the gas-coupled UT sensor will be 0.25” (~6 mm), which should be readily attained. Initial sensors in this report were 10 mm diameter. Liquid coupled ILI tools use ceramic UT sensor sizes on the order of 0.25” to 0.375” in diameter. Ideally the system would provide a sampling density finer than the sensor diameter.

GTI noted in the analysis that the percent depth to thickness ratio (%d/t) for failure approaches approximately 18% for longer flaws (on the order of 5” to 6”). If the wall thickness is 0.25”, this represents wall loss of 0.045”. This suggests that the single crystal UT sensor would need to have a thickness measurement resolution of approximately 0.005” = 0.13 mm (~10x resolution). This target sensor resolution is reflected in Table I. Both the target wall thickness measurement resolution and the sample spacing are consistent with the corrosion data provided by GTI.

Operations Technology Development (OTD) took responsibility for formation of a technical advisory group (TAG). A TAG meeting was held on May 24, 2017 hosted by OTD and including participants from Duke Energy, PG&E, SoCal Gas, Southwest Gas and NySource.

PZT Crystal Growth Development, Fabrication and Scale Up

Summary

Lead zirconate titanate (PZT) is overall the most efficient and effective material for high power transducers and it is used in countless applications in the form of a sintered ceramic (often inaccurately called a crystal), which was previously the only commercial form of PZT available. Recent data on small flux-grown PZT crystals from Xie et al. [1,2] give an existence proof that single crystals of PZT could fulfill higher transducer/receiver efficiency goals compared both to ceramics and other low-power, low-temperature single crystals such as PMN-PT, but their method is not scalable or able to be commercialized and only a few small samples were made. Single crystal transducer prototypes have shown an efficiency improvement of 3x over ceramics on both send and receive, resulting in approximately an order of magnitude increase in system sensitivity.

Lead zirconate titanate ($Pb(Zr_xTi_{1-x})O_3$) is a solid solution perovskite between the end members lead titanate ($PbTiO_3$—PT) and lead zirconate ($PbZrO_3$—PZ). The optimum composition is near equimolar $PbZr_{0.52}Ti_{0.48}O_3$ at what is called the morphotropic phase boundary (MPB) where the dielectric and piezoelectric properties have a sharp maximum. PZT is non-congruent, meaning it cannot be grown from a melt of the same composition. Attempts to grow this material by flux/solution growth have been made over more than fifty years, but to date only small, non-uniform, poor quality crystals, often off the ideal MPB composition, have been achieved by non-scalable methods owing in part to the constraints of three-dimensional growth from a point nucleus, the difference in solubility between TiO_2 and ZrO_2 and unstable growth conditions caused by high flux evaporation and selective depletion. In this set of tasks, prototype PZT crystals are being grown from high temperature solutions (HTS) with a newly invented custom flux.

Enabling technologies that had to be developed include:

- Development of an innovative flux with a low vapor pressure and high solubility.
- Development of x-ray diffraction (XRD) techniques to measure the crystal composition precisely.
- Calculation and modeling of the phase diagram.
- Putting the flux and phase diagram together to show they uniquely provide a region where the desired near-equimolar composition can be grown without phase separation compared to previous fluxes.
- Developing calculation tools to determine growth conditions and crystal composition for any starting melt composition.
- Observation of step bunch and avoidance of macro-steps during the microscopic process of crystal growth.
- Avoidance of cracking through the elimination of strain in the crystal.
- Development of initial PZT seed growth on platinum.
- Seed orientation to maximize surface quality and fraction of usable crystal.
- Growth rate optimization through melt size/crystal size and temperature ramp to smooth the growth surface and achieve compositional uniformity.
- Developing a method of crystal orientation and fabrication for characterization and transducer manufacture.
- Eliminating trapped flux inclusions.

- Scaling up the processes to large crystals.
- Determination of an optimum target PZT composition with highest performance from feedback based on measurements at Penn State.

This work has developed the process from sub-millimeter crystals to large crystals greater than 2 cubic centimeters for characterization and transducer manufacture scaling up by a factor of over 500 in size. A second furnace has been brought on line to increase capacity.

Qi2 History of High Temperature Solution (HTS) Growth of PZT from a Flux

In earlier work funded internally and with a grant from Chevron, Qi2 established a superior flux and initial melt composition for growth of PZT single crystals with 1) good solubility of PZ, 2) reduced volatility, 3) reduced growth temperature, 4) no second phase formation or phase separation and 5) a moderately uniform crystal composition. Preliminary solubility relations were developed using both ideal and regular solution theories. Figure 3a shows light yellow PZT polycrystals from the process and Figure 3b shows a micrograph of separated cubes less than 1 mm in size. This was the state of Qi2's PZT crystal growth research at the outset of this project.

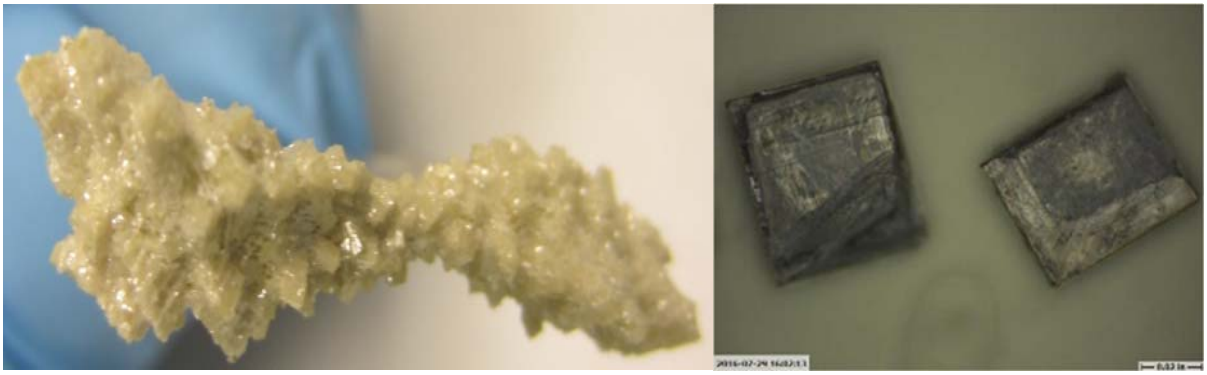

(a) (b)

Figure 3. (a) Photograph of as-grown PZT polycrystals on the stirring paddle with a yellow appearance. (b) Micrograph of single crystal cubes separated from the polycrystal mass. These appear dark because of the microscope lighting.

Based on this work, Qi2 was able to file U. S. Patent 9,738,990 "Method of Growth of Lead Zirconate Titanate Single Crystals," that was issued August 22, 2017 and contains extensive further details on the process. This information was used to establish the necessary equipment and supplies for this project and they were acquired and inventoried.

Compositional Determination

To determine the phase diagram, it was first necessary to get data pairs of the crystal composition x(crystal), where x is the Zr fraction in $Pb(Zr_xTi_{1-x})O_3$, versus the melt fraction x(melt). This required a good analysis method for crystal composition. There are a number of conventional compositional analysis methods such as x-ray fluorescence (XRF), but experience has shown those data have a limited number of significant figures insufficient for this determination. More often, properties measurements can be more accurate. An x-ray diffraction (XRD) method was therefore developed to determine the composition from the XRD line positions as follows.

The XRD Powder Diffraction File[3] cards were analyzed and tabulated for all PZT compositions representing d-spacing data for diffraction lines at various compositions x(crystal) including end members lead zirconate (PZ) and lead titanate (PT). The d-spacings were plotted versus composition for the various lines to determine slope and intercept for each. For some lines such as (111) there was a continuous line through all compositions, but most required separate fits for the tetragonal and rhombohedral regions. Some had a reasonably high slope and were sensitive to composition variation, but some had such low slope that there was insufficient variation to be useful in composition determination. A template file was constructed to show all the lines both tetragonal and rhombohedral. These formulae could be inserted into the XRD file for any given crystal and the composition determined to a high accuracy by averaging their results.

Top Seeded Solution Growth (TSSG)

TSSG allows the crystal grower to bootstrap from seeded growth on a completely different material (heteroepitaxy), in this case a platinum paddle, rod or wire, to homoepitaxy on a PZT seed thus created. Results showed that HTS growth on platinum can be viable for creation of an initial seed because platinum is a good nucleation site and it does not dissolve in the melt. Platinum has long been used as a buffer layer in growing piezoelectric perovskites on silicon, where the resulting epitaxy is textured polycrystalline with grain boundaries and dislocations to accommodate the mismatch rather than being a true single crystal. Earlier growth runs on the platinum paddle (e. g. Figure 3a) were highly polycrystalline showing the many orientations of platinum grains in the paddle.

Platinum has a moderate lattice match to PZT with a room temperature cubic lattice parameter of 0.392 nm, 3.7% lower than the PZT average and, in fact, worse than some substrates tested. This persists to high temperature, but it wins the competition because, unlike oxide substrate materials, it does not dissolve, so the growth interface can only move one way. However, there is the issue of how the lattice mismatch affects the nucleation and growth rates and the required undercooling. Surprisingly only an extra 4-5°C undercooling is required to nucleate on platinum.

Continuous development of TSSG has proceeded through the contract, including the following aspects:

- Flux composition ratios
- Nutrient concentration in the melt
- Ti/Zr ratio in the melt
- Crucible size
- Melt size
- Size of crystal grown
- Equilibration temperature and time
- Saturation temperature
- Growth temperature
- Thermal gradient
- Temperature profile for growth
- Initial supercooling
- Location of temperature control thermocouple on winding

- Location of temperature monitoring thermocouple in the furnace
- Pedestal height
- Insulation at the bottom of the furnace
- Baffling to control thermal convection and flux evaporation

The growth method has been modified to suppress extraneous nucleation and promote growth of larger PZT crystals. Crystals over 2 cubic centimeters in size have been grown, fabricated for transducers and fully characterized.

Crystal Orientation and Fabrication

A set of at least two opposing, oriented, polished crystal faces is required for piezoelectric characterization and transducer fabrication. The PZT crystals obtained in this project are faceted along the <1,0,0> family of directions, which is also the desired direction for transducer plates. Crystals were initially oriented visually using these facets. Lacking a Laue x-ray system, a method was developed to orient crystals within the required tolerance on a powder diffractometer using an inexpensive in-house designed and manufactured 3-axis goniometer (Figure 4). Small motions were made around this visual orientation to obtain a diffraction maximum. Surprisingly, this was possible in 5-20 iterations without taking excessive time. The goniometer could then be transferred directly to the saw for oriented cutting within the required tolerance. In general, the procedure was most amenable to cutting one oriented flat face and then using that to hold/orient the crystal. Lapping/polishing the opposite face proved more effective than sawing, since care could be taken to remove only the right amount of material to a precise thickness and the lapped/ polished face could be progressively examined for quality during the process.

Figure 4: In-house designed and manufactured 3-axis goniometer.

A small outer diameter (OD) ceramic saw was used to cut the single crystals out of the polycrystalline matrix or as-grown TSSG single crystal. New fixturing was required to mount the crystals and translate them across the saw blade to obtain a crystal with right angle corners and sides aligned to the crystallographic directions. This cutting was performed in a dedicated fume hood for processing PZT that is connected to a packed bed scrubber that services all aspects of the growth and fabrication applications for employee safety and environmental compliance.

When a crystal (or a ceramic for that matter) is cut, lapped or polished with a grit of some size, the grit does damage to the crystal. Thus, this process uses sequentially smaller grits to eliminate as much damage as possible. A typical surface finish (Ra) for ceramic PZT is Ra < 0.7 μm and, surprisingly, American Piezoelectric Corporation (APC) uses ~320 grit (44 μm particle size) to get a Ra < 0.7 μm finish in ceramics.[4] A specification for PMN-PT single crystals can be Ra anywhere from 0.2 μm (near mirror) to 1 μm (USDA bead blasting). Qi2 does lapping/polishing of optical components on a regular basis and these require a higher degree of finish than piezoelectric materials. The current process uses coarse and fine commercial sandpapers down to 2000 grit to

get an adequate finish. The crystals were lapped and polished to shape and for thickness tuning and surface finish. We constructed an in-house made lapping jig that could maintain orientation and flatness during the lapping and polishing process. More recently, edge polishing of samples 2x2x0.3 mm was developed to fabricate "splinter" samples for additional piezoelectric properties measurements and transducer crystals have been fabricated from the largest pieces.

The initial crystals had an additional problem that appeared in the fabrication phase. The crystal growth angles in the seed are fairly random and so the crystals that grew had crystal planes oriented at a significant angle 30-45° to the planar direction. Thus, any crystal cut from this material had to be cut at a sharp angle and that had to be trimmed further to eliminate the outermost portions resulting in a much smaller fabricated crystal as shown in Figure 5a. The solution has been to orient the seed so the planes of the crystal are nearly parallel to the surface of the melt. Thus, the laterally growing crystal has the crystal orientation nearly aligned with the plane of growth as shown in Figure 5b.

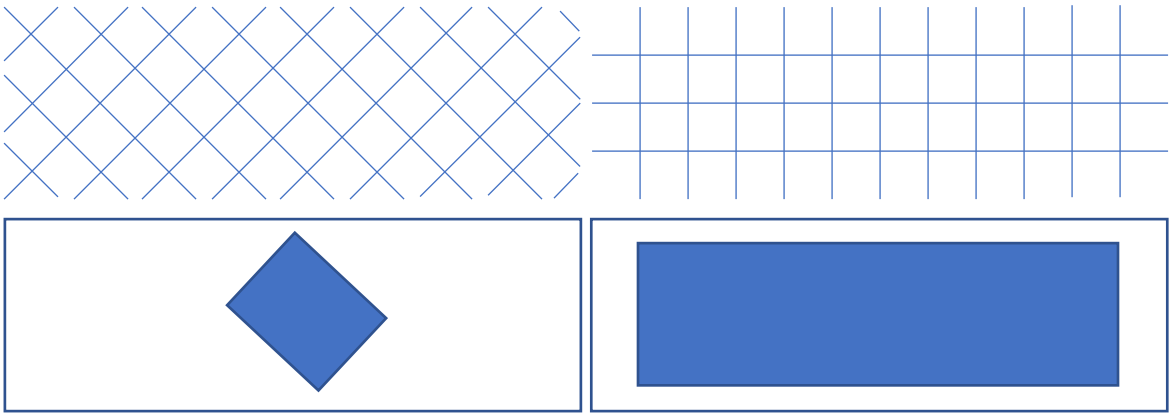

Figure 5: a) Planar crystal with oblique crystal orientation. b) Planar crystal with planar crystal orientation. Blue rectangles indicate the rectangular oriented crystal sample that can be fabricated from this orientation.

Liquid Phase Epitaxy (LPE)—Heteroepitaxy on a Structure/Lattice Matched Substrate

PZT was previously grown slowly in thin film form by vapor phase epitaxy, but liquid phase epitaxy was not previously achieved in any bulk or thick film form that would be useful for a transducer. Other HTS techniques, such as slow cooling over a wide temperature range, caused the thermodynamic conditions and the crystal composition to vary too much. LPE (depicted atomistically in Figure 6a and pictorially in Figure 6b) is a near-equilibrium HTS growth

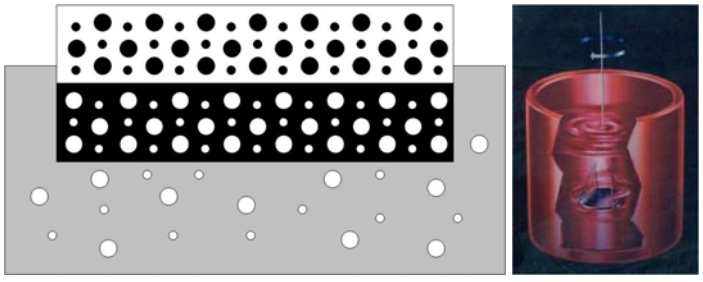

Figure 6. a) Schematic depiction of LPE at the atomistic scale. b) Drawing of LPE furnace growth.

technique that achieves high crystal quality comparable to the substrate if there is a good match of structure, lattice parameter and coefficient of thermal expansion between film and substrate. LPE has a high volumetric growth rate because the crystal only needs to grow outward in one dimension and has higher growth rates than vapor phase growth. It is conducted at near-constant growth conditions to yield uniform compositions. The substrate is lapped off after growth of a thick film for a free-standing crystal plate.

Substrates

Key to performance of liquid phase epitaxy is the substrate, which provides a template for growth. Congruently melting substrate crystals growable by some large-scale bulk process such as the Czochralski method or Bridgman can be matched up with non-congruent film compositions that must be grown by epitaxial techniques to produce film/substrate combinations with effective composite properties. To grow quality epitaxial crystals and, in many cases, to grow the desired phase at all, the film and substrate must have an acceptable match in structure, chemistry, lattice parameter and coefficient of thermal expansion, although there are some notable exceptions such as the use of platinum described earlier. The substrate must be of good crystal and surface quality since any defects will normally propagate into the film. It should have no phase transition between room temperature and the epitaxial growth temperature. For a commercial technology, the substrate material should be able to be grown ≥50 mm in diameter or square dimensions and have low cost. This is obviously a very significant set of constraints that was challenging in the present case. Figure 7a depicts a Czochralski-grown boule of a perovskite substrate material[5] and some sliced, but unpolished substrates are seen in Figure 7b.

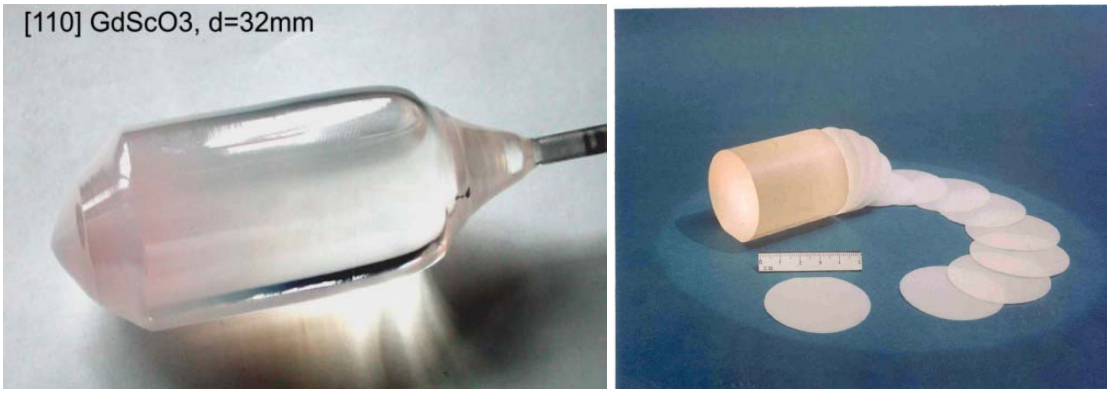

(a) (b)

Figure 7. (a) Boule of the perovskite substrate material gadolinium scandate.[5] (b) Sliced but unpolished substrates cut from a boule.

New Substrate materials

There are limited choices of perovskite crystals that can be grown as uniform crystals in bulk form. As can be seen from Figure 8, there are substrate candidates with primitive perovskite lattice parameters from 0.367 to 0.417 nm, however from 0.403 to 0.412 nm, which is desirable for lattice matched growth of PZT, there is a dearth of materials and perovskites such as the rare earth scandates, $KTaO_3$ and $SrTiO_3$ with lattice parameters 0.390 to 0.402 nm are difficult and expensive to grow. Therefore, a program was initiated to invent new substrate materials.

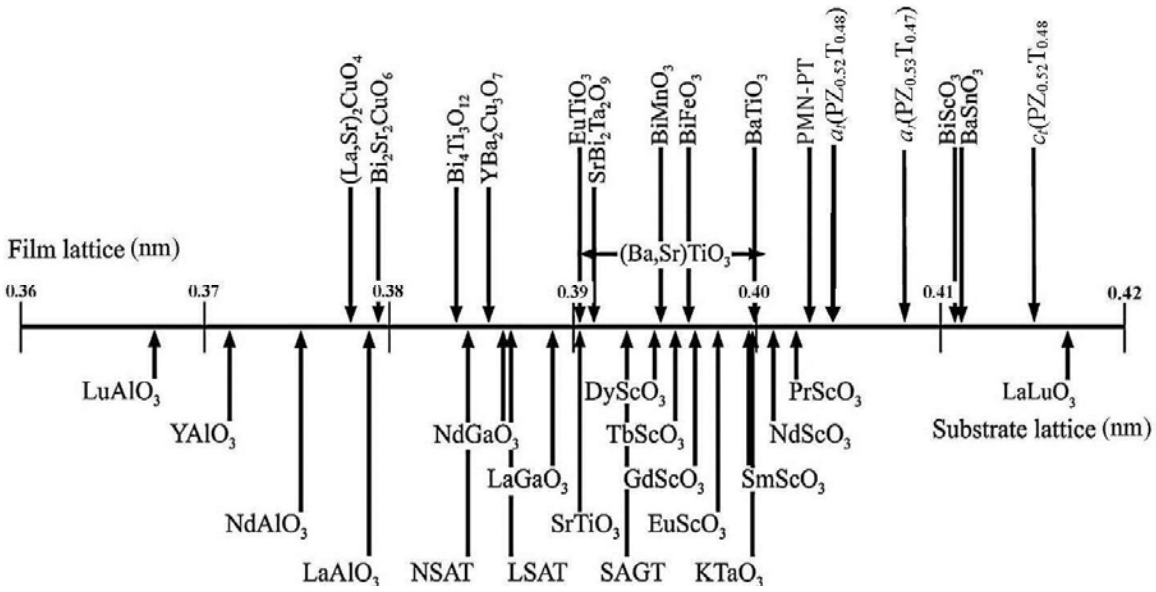

Figure 8. Prior art plot of known substrate materials (bottom) and some desired film materials (top) plotted on the average lattice parameter number line for the simple perovskite single formula unit ABO_3 unit cell.[6] *The rare earth scandates technically have an orthorhombic crystal structure, but can be grown such that they have an effectively square lattice growth plane with the indicated planar lattice parameters a_p.*

New congruently melting solid solutions have been invented under this research program.[7,8] Bridgman growth was attempted of a solid solution between perovskites $NaNbO_3$ (NN) and $BaLi_{0.25}Nb_{0.75}O_3$ (BLN) with collaborators at Florida State University.[7] Crystals were seen in the bottom of the crucible. The charge broke up as the crucible was removed and the full size of the crystals is not known. Pictures of broken pieces removed so far are shown in Figure 9.

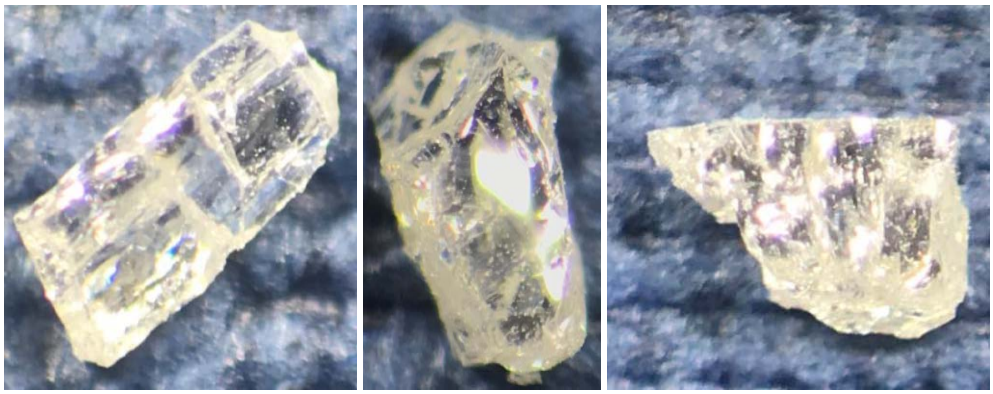

Figure 9: Small $0.41NaNbO_3$-$0.59BaLi_{0.25}Nb_{0.75}O_3$ crystals extracted from a Bridgman crucible.

The crystals are water white and display no issues with Nb reduction. A single crystal lattice parameter was determined to be 0.410958(5) nm, which is slightly larger than the value of 0.4098 nm determined from powder diffraction of sintered samples and Nelson-Riley extrapolation.

Czochralski and analysis work has begun on this system at IKZ in Berlin. The first Czochralski run (unseeded—Figure 10) produced a well-formed boule ~14 mm in diameter with three separate crystals and some cloudy areas.[7] Further work using a seed cut from this crystal is expected to improve this, but initial substrates could be fabricated.

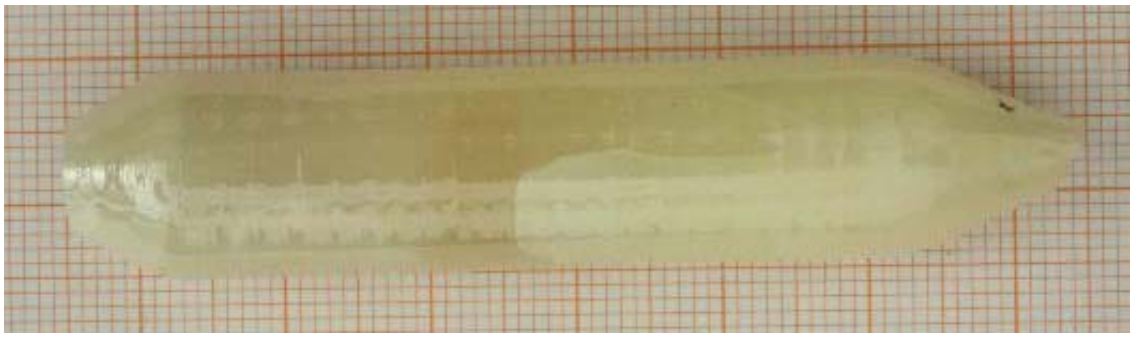

Figure 10: Initial Czochralski boule grown from the NN-BLN system. Three separate crystals can be seen along with various degrees of cloudiness, likely from second phase.

Crystal doping

PZT is a ferroelectric perovskite, whose properties can be altered by doping with ions of different valence from the base $Pb^{2+}(ZrTi)^{4+}O_3$ lattice. Understanding doping has been seen to be completely intertwined with characterization.

"Soft" PZT can be doped with donor dopants: e. g. La^{3+} for Pb^{2+} or Nb^{5+} for Ti^{4+}/Zr^{4+}. A donor dopant is one that has a higher valence than the ion it is replacing so it can donate an electron unless it is suitably compensated by a cation vacancy. Donor dopants create lead vacancies and are used to make soft PZT, which is not what is desired in this application.

"Hard" PZT, as is desired here, is typically doped with an acceptor dopant of lower valence such as Fe^{3+} or Mn^{3+} (potentially multi-valent, e. g. Fe^{3+}+Fe^{2+}) substituting for Ti^{4+}/Zr^{4+} so it can accept an electron unless it is compensated by an oxygen vacancy. The literature shows that the tetragonal distortion embodied in the ratio between the lattice parameters c/a determined by x-ray diffraction is a significant indicator of Fe or Mn substitution. Figure 11 shows that Fe has a c/a versus concentration slope of -0.270 near the origin, but there is a change in effect with higher concentrations, which are typically considered above the solubility limit.

We doped the melt with Fe/(Zr+Ti) fractions of 0.003, 0.007 and 0.010 and grew crystals that were then characterized by powder x-ray diffraction. After extensive review of the resulting crystal structure data, we were able to determine the following.

- Fe goes into the crystal mixed valence as Fe^{3+}/Fe^{2+} in approximately equal proportions. This is expected from the iron oxide thermodynamics and phase diagram. The average ionic size of Fe substituents is 0.8525 Å, which is very close to the ionic size of Zr^{4+} 0.86 Å.
- Fe substitutes preferentially for Ti rather than Zr. This is logical since Zr has a higher distribution coefficient, is more refractory and is hard to compete thermodynamically.
- The combination of these effects is that, in addition to introducing oxygen vacancies, Fe has the same effect on the crystal structure as adding more Zr, including moving the

tetragonal-rhombohedral phase boundary and changing c/a. These results are not found in the literature and represent a new understanding. This has allowed determination of the Fe concentration in the crystal from the difference between the expected crystal structure (lattice parameters c, a and their ratio) based on the known Zr distribution coefficient and the observed crystal structure.

- The thus calculated Fe concentration in the crystal is plotted for the three different melt doping levels in Figure 12. The results are surprisingly uniform with a distribution coefficient of 2.4. If calculated only from the Ti concentration, for which Fe substitutes, in the film versus the melt, the distribution coefficient closer to 4, which is quite high.

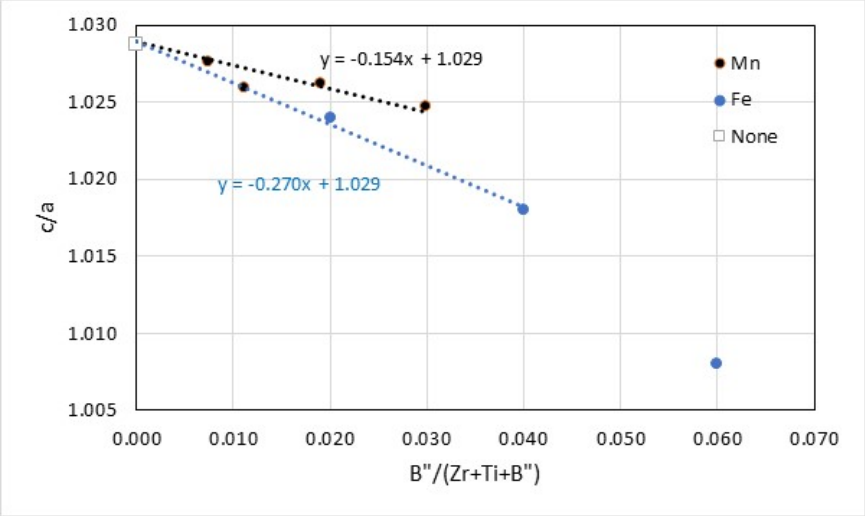

Figure 11: c/a lattice parameter ratio for Mn and Fe doping in PZT.

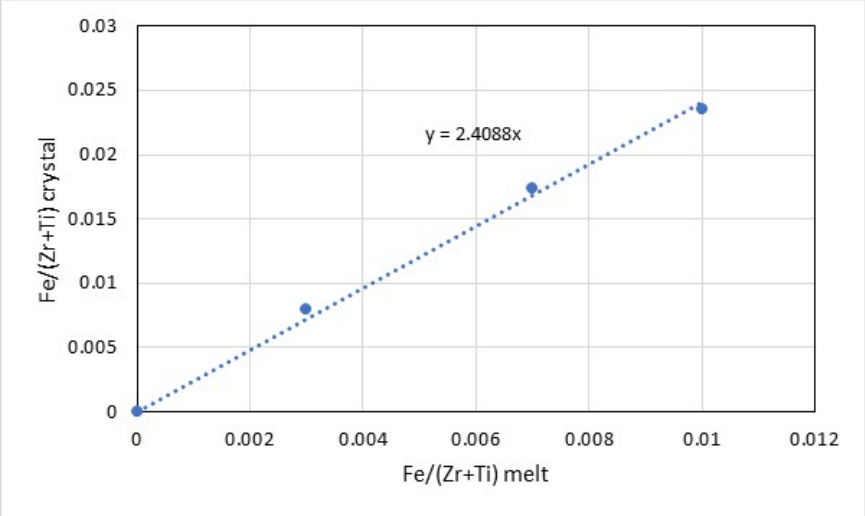

Figure 12: Calculated Fe concentration in the crystal (based on structure variation) versus melt concentration with respect to B-site ions.

This strong effect of iron doping is cautionary in that any iron impurity in the melt will cause the crystal to deviate significantly in structure and properties.

It was therefore seen that growth of doped crystals under these conditions is more problematic than preparing a doped ceramic. A doped ceramic may be made with a specific and uniform dopant concentration by careful weighing and mechanical mixing and grinding using the usual ceramic preparation techniques. The high distribution coefficient of dopant in melt growth results in rapid melt depletion and variation of the doping level through the crystal. Because of the strong effect of doping, this will result in a crystal with extremely non-uniform properties.

However, the current characterization results below have shown a solution. Because a principal effect of the dopant is to reduce the c/a ratio in the crystal, it was hypothesized that doing this by changing the Zr fraction could have the same effect. The Zr fraction in the crystal was changed by 1% and the resultant crystal had distinctly changed properties. To quote our collaborator Prof. Susan Trolier-Mckinstry at Penn State "The last crystal grown appears to be acting like a hard PZT ceramic."[9] Therefore, this material is shown to be an effective realization of a hard PZT single crystal without actual doping. This method cannot work in a ceramic because there is microscopic phase separation that is avoided in the single crystal.

Crystal Characterization

To summarize the characterization results, the performance of the new single crystals is already much better than conventional ceramics, particularly hard ceramics and there appears to be room to improve further. The d_{33} numbers are triple the hard piezoelectric ceramic values.

First, we will discuss the prior art in PZT properties. The original undoped PZT ceramic relative permittivity and d_{33} data were taken by Jaffe[10] (orange in Figure 13) showing the peaks in both at the morphotropic phase boundary (MPB). Recently Xie et al.[1,2] grew small single crystals of PZT in a range of compositions (red in Figure 13). The peak width of both ε and d_{33} are broadened in the ceramic, most likely because of microscopic phase separation.

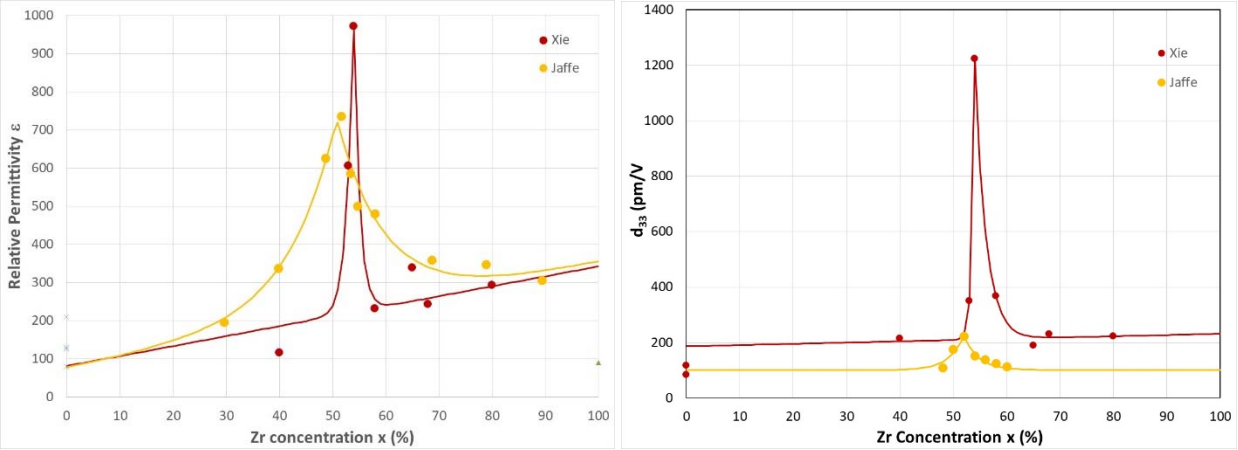

a) b)

Figure 13. a) Relative permittivity ε and b) piezoelectric coefficient d_{33} data for ceramics[10] (orange) and single crystals[1,2] (red) of varying compositions. The fits are asymmetric Gaussians.

The large difference in the magnitude of d_{33} is the motivation for the current development of single crystals and the performance we are trying to match. The peak position for Xie's data is offset by 2% from the standard MPB value for reasons that are not understood by us.

Single crystal characterization, based on the IEEE standard on piezoelectricity was performed by Professor Susan Trolier-McKinstry's group at The Pennsylvania State University (Penn State). All rights to data were assigned to Qi2. Four lots of improved quality crystals fabricated with (100)/(001) orientation have been delivered and measured.

Characterization was focused on the piezoelectric coefficient d_{33} in both the unpoled and poled state (measured in pm/V, which is the same as pC/N), coercive field E_C, the relative permittivity ε (also known as dielectric constant) at the standard 1 kHz frequency, dielectric loss tangent tan δ also at 1 kHz, Zr concentration x in $PbZr_xTi_{1-x}O_3$ and crystal quality and alignment. Specifically, the following measurements have been made.

1. Powder x-ray diffraction of ground edge pieces to determine composition. (Qi2)
2. Single crystal x-ray diffraction to determine degree of alignment. (Penn State and Qi2)
3. P-E (polarization-electric field) hysteresis loops were measured. (Penn State)
4. Unipolar and bipolar strain (S-E) loops were measured. (Penn State)

Figure 14 shows the XRD data taken at Penn State on the best performing Qi2 sample. At the higher angles there is better resolution and three split peaks can be seen indicative of being at the desired morphotropic phase boundary with unstable crystal structure. These can be interpreted as being from the (x00)/(00x) tetragonal and (x00) rhombohedral phases or all resulting from a more complex monoclinic phase.

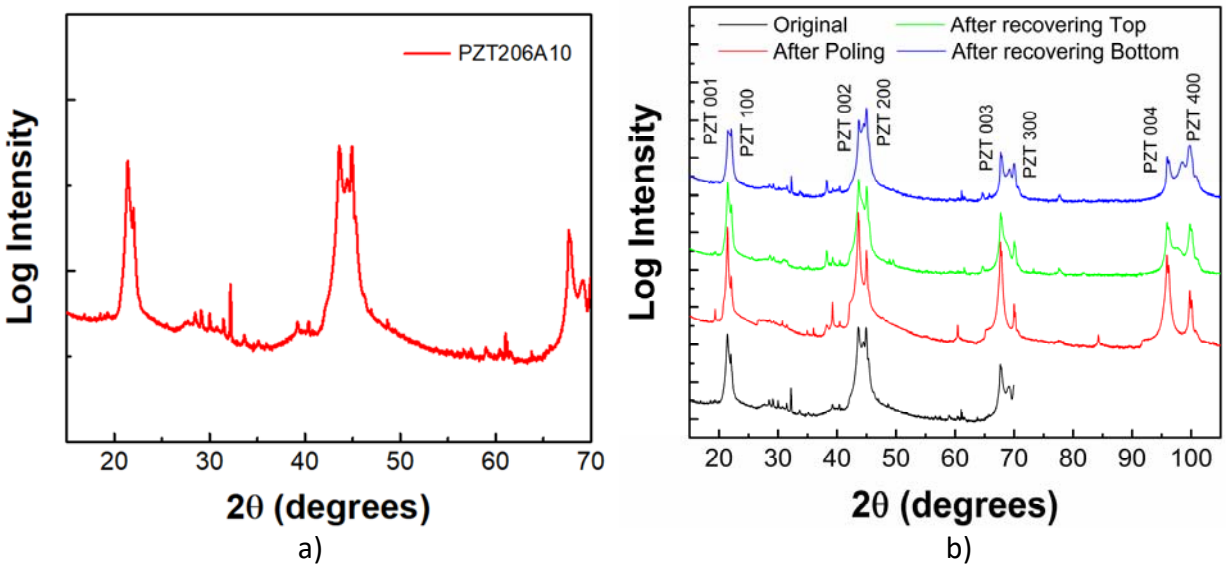

Figure 14. This sample was fabricated along the (100)/(001) direction. Three spilt peaks can be found at {200}, and {300}. The rhombohedral phase disappeared after poling, and appeared again after a recovering bake (420℃ for 30 min) above the Curie temperature.

When the material is poled, the (x00) rhombohedral lines disappear, but when the poling is eliminated (recovered) by annealing above the Curie temperature, those lines return and can be seen on both the top and bottom of the sample. This shows uniformity and gives an indication of how the material will perform in applications when it will typically be poled.

Full bipolar hysteresis loops and unipolar displacement loops were taken for the samples both unpoled and poled to extract the desired data. Figure 15 shows the loops and data for the best sample.

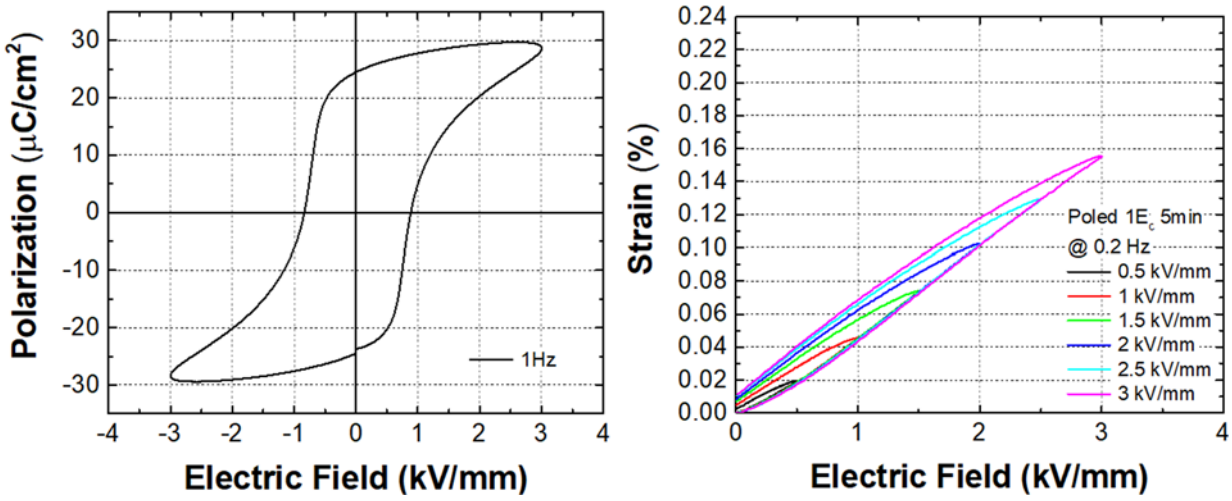

a) b)

Figure 15. Bipolar hysteresis loops and poled unipolar displacement loops for the best PZT single crystal. Data taken from these plots include: relative permittivity ε = 492, loss tangent tan δ = 0.028 @ 1 kHz, calculated d_{33} = 717 pm/V (unpoled), 727 pm/V (poled).

Figure 16 shows the relative permittivity and dielectric loss as a function of temperature and frequency. The permittivity peak occurs at the Curie temperature T_C.

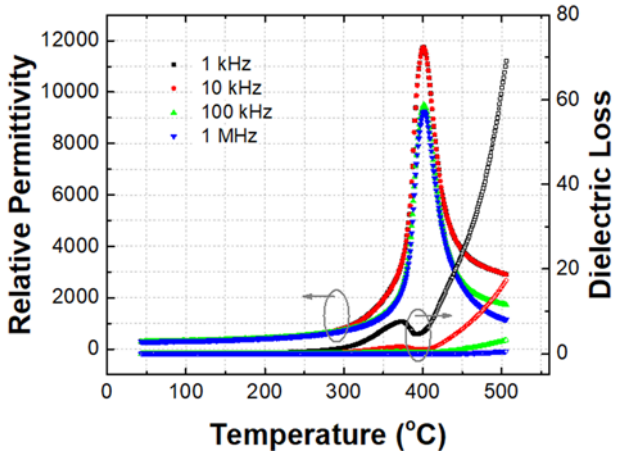

Figure 16. relative permittivity and dielectric loss as a function of temperature and frequency in the PZT single crystal.

Electrical measurements were also taken on a slab from another PZT single crystal in Figure 17 to determine the necessary electrical control conditions.

This was the sample with higher Zr content and was shown to be similar to a hard PZT ceramic such as PZT-5A with comparisons and calculated values from the resonances in Table II. However, the d_{33} of this material is significantly higher, 598 pm/V for this single crystal compared to 350 pm/V for a PZT-5A ceramic, reflecting the improved efficiency of the single crystal.

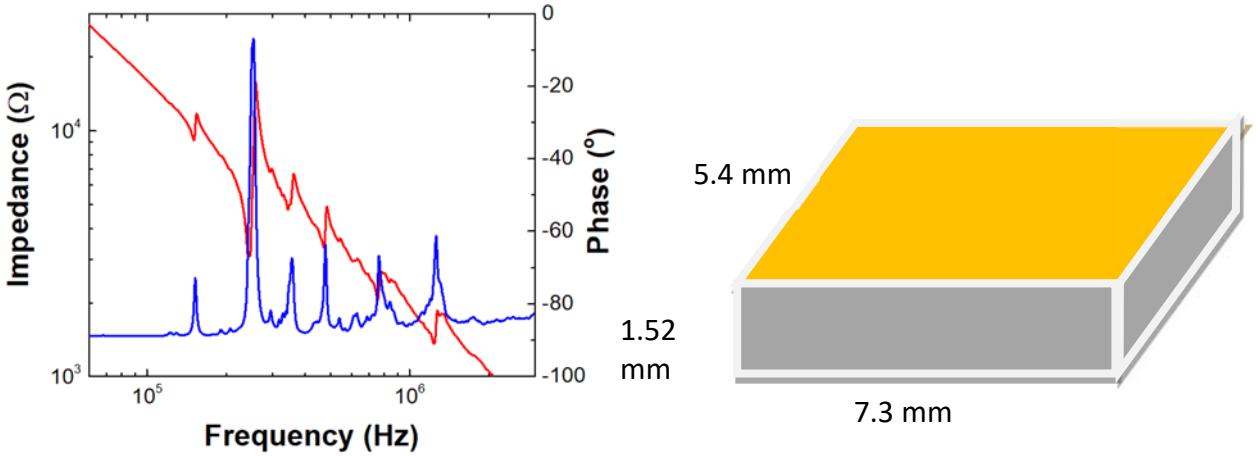

Figure 17. a) Electrical impedance and phase of hard PZT single crystal vs. frequency with resonance peaks at 1: 153 kHz, 2: 254 kHz (7.3 mm), 3: 356 kHz (5.4 mm), 4: 477 kHz, 5: 763 kHz, 6: 1.26 MHz (thickness 1.52 mm). b) Dimensions of the resonant plate are shown

Table II. Comparison of 1) frequency constants between the hard PZT single crystal and PZT-5A ceramic, 2) measured versus calculated resonance and 3) mechanical properties.

	Frequency Constants PZT-5A, (mHz)	Frequency Constants PZT crystal (mHz)	Calculated Resonance Frequency (kHz)	Measured Resonance Frequency (kHz)	Mechanical Coupling coefficient	Mechanical Quality Factor Q_M
Radial N_r (7.3 mm)	2,000	1,854	273	254	k_r = 0.344	11
Radial N_r (5.4 mm)	2,000	1,998	370	356	k_r = 0.344	13
Thickness N_t (1.52 mm)	1,800	1,794	1,180	1,260	k_t = 0.265	18.7

Table III compares Penn State's results to earlier results on small PZT single crystals by Xie et al.[1,2], a calculated PZT single crystal d_{33} from phase-field simulation[11], literature data on undoped PZT ceramic[12] and standard data on doped PZT ceramics[13]. The doped ceramics may be quite different

in composition from pure PZT and are standardized to Navy requirements by properties rather than composition.

Table III – Piezoelectric, dielectric and structural properties of PZT single crystals compared to the prior art (italics). Single crystal (sc) literature data (measured and theoretical) are in blue and ceramic data are in red including undoped pure PZT.

Sample	**d_{33} (pm/V)**	**E_C (kV/mm)**	**ε @1 kHz**	**tan δ @1 kHz**	**T_C (°C)**	**x**	**Comments**
PZT206A10	727	1.27	492	0.028	401	0.522	Qi2 single crystal
PZT209A5	598	0.86	364	0.036		0.534	Qi2 single crystal
PZT-sc Xie[1,2]	*1223*	*1.7*	*971*	*0.0065*	*394*	*0.54*	*Undoped*
PZT-sc th.[11]	*720*				*~400*	*0.53*	*Undoped*
PZT ceramic[12]	*220*		*730*	*0.004*	*310*	*0.52*	*Undoped*
Navy III[13]	*215*	*1.5*	*1050*	*0.004*	*250*		*Hard doped PZT*
Navy VI[13]	*630*	*0.8*	*3300*	*0.025*	*120*		*Soft doped PZT*

The d_{33} numbers represent the efficiency of the piezoelectric material in terms of conversion between electrical power in and ultrasonic power out and vice versa and are quite good both by our understanding and Prof. Trolier Mckinstry. The poled numbers are equal to the calculated value, triple the hard-doped ceramic number and higher than the best soft doped ceramic. The unpoled data are higher because the measurement picks up domain switching that can't be used in practice. The poled numbers are more relevant to applications and are very consistent. The best poled data is in the largest, highest quality and best oriented crystal and the poled and unpoled data are almost identical tending to confirm the high crystal quality from the absence of defect domains more likely to contribute to switching in unpoled material. The d_{33} data are much better than in ceramics, but not yet quite as good as Xie's unconfirmed report. It is unknown whether Xie's data are poled or unpoled.

The coercivity data is similar to Xie's and as good or better than doped hard PZT ceramics indicating that doping is possibly not needed for good transducers.

The current relative permittivity data seems consistently around 490, 28% less than the 730 of undoped PZT ceramic and 46% lower than Xie's 971. We are investigating what might contribute to this, but it is most likely the compositional gradient of ±2% in the crystal overlaid on the sharp permittivity peak shown in Figure 13.

The loss tangent is a bit high as would be expected until the crystals are of the highest quality. It noticeably decreased in the last three samples where measures were taken to improve crystal quality and there it is as good as in soft PZT ceramic.

Prof. Trolier-Mckinstry characterizes the quality of the crystals as similar to early crystals of PMN-PT at the same stage of development. The crystal compositions are very consistent near the target of slightly under the MPB composition x = 0.52.

The relative permittivity and d_{33} of all the Qi2 samples are plotted and compared to the data for Xie et al.[1,2] across a range of compositions in Figure 18. Because of the offset of the data of Xie, it was necessary to offset the Qi2 data by a corresponding amount to fit the results.

These plots show that the lack of matching with the best of Xie's data may originate in 1) imprecision of composition with a slightly lower composition being required or 2) a compositional gradient in the sample, which would result in an average value around the sharp peak, similar to the data of Jaffe in Figure 13.

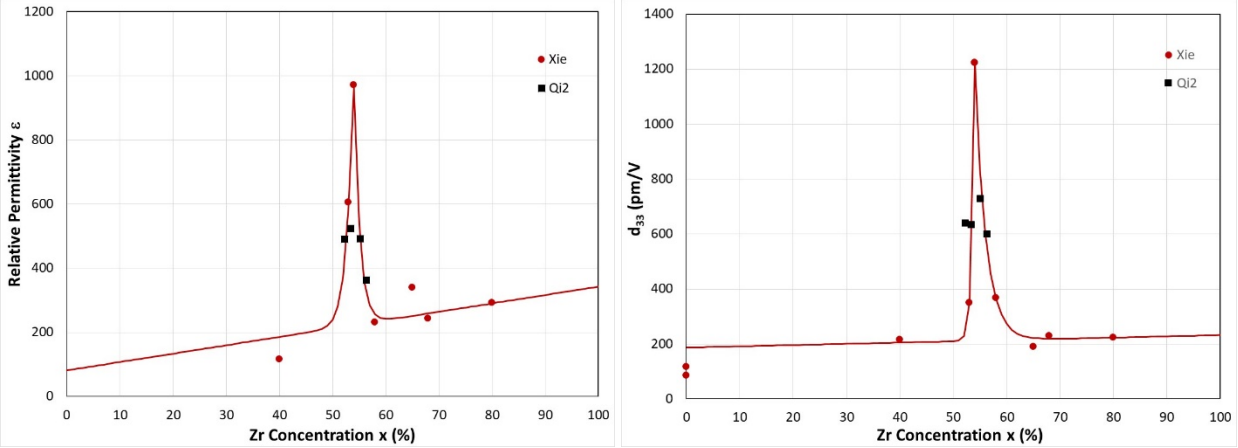

Figure 18. Relative permittivity ε and piezoelectric constant d_{33} of all the Qi2 samples plotted and compared to the data for Xie et al.[1,2]. The Qi2 data had to have a fitted offset to match because of the offset of the previous data from the standard MPB value.

Transducer design

Figure 19 shows a conventional transducer design. It was not the intent to reinvent this completely, but the basic design was retained and design improvements have focused on the transducer elements that will differ significantly from the current state of the art.

- Piezoelectric element
- Impedance matching coatings
- Backing material

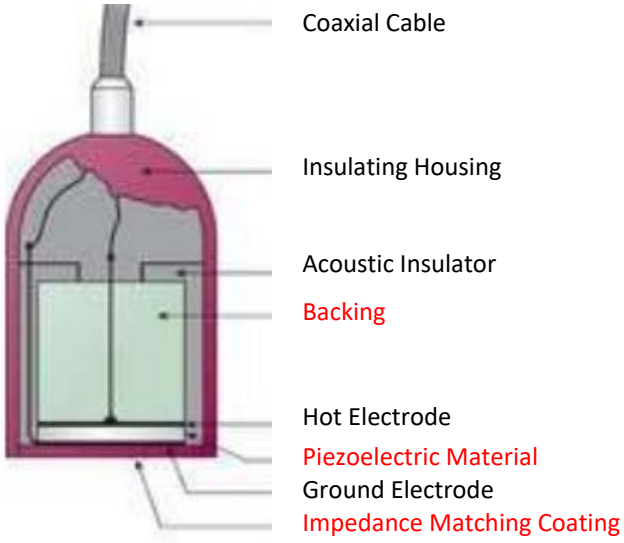

Figure 19: Schematic of an ultrasonic transducer.

The current development of single crystal PZT discussed previously will have immediate improvements in performance of the piezoelectric element because the higher efficiency and improved coupling constants of single crystals will permit larger surface motions of the transducer and more effective coupling and energy transfer to gas/air.

Further improvement of the transducer performance principally revolves around impedance matching to air/gas. The acoustic impedance Z of a material is given by the density times the speed of sound in the material, $Z = \rho c$. Table IV gives acoustic impedances for some relevant materials.

Table IV: Acoustic impedance Z of some materials.

Material	Z (MRayl = 10^6 kg/s/m^2)
Natural gas (1 bar = 14.7 psi))	0.0003
Natural gas (500 psi)	0.0126
Air or nitrogen (1 bar)	0.000425
Air or nitrogen (500 psi)	0.015
Crude oil	1.3
Water	1.48
Epoxy (depending on fill)	~3 average (0.88-9.45)
Solid PZT ceramic	34.2
Steel	39

As is well known, sound attenuation in air increases with increasing frequency and is significant above 2 MHz. Per Blomme[14], at 1 bar atmospheric pressure "in practice ultrasound of 1 or 2 MHz can propagate in air for a distance not more than a few centimetres." Conversely, the resolution of a thickness tool is inversely dependent on the frequency. One of the goals of this project is to measure pipe thickness down to ¼" (~6 mm) minimum thickness, which ideally requires a frequency of 3-4 MHz to observe the first back wall reflection. These two factors must be balanced in a device for gas-coupled non-destructive evaluation (NDE). 1 MHz is commonly the highest frequency for prototypes in 1 bar atmospheric pressure, so that was adopted for the first round of transducers. However, for higher pressures inside the pipes (around 17-55 bars or 250-800 psi), there is less attenuation and 2-4 MHz frequencies can be targeted. The attenuation of a gas scales approximately inversely as the density and inversely as the square of the frequency. Obviously, the total magnitude of the attenuation will also strongly depend on the standoff. Qi2 compared two types of gas-coupled transducers at a 30 mm standoff, a commercial Ultran transducer (2.5 MHz) and a transducer developed under this project (2 MHz). At 500 psi, these would respectively have relatively small 0.9 dB and 0.33 dB attenuations compared to 30.6 and 11.1 dB at 1 bar. Therefore, the use of even reasonable pressure is highly enabling for higher frequency transducers. However, at these frequencies, the wavelength is inversely proportionally lower and quarter-wave coating materials can become unworkably thin or unavailable. This has been a primary barrier to moving to higher frequencies.

The basic physics of anti-reflection coatings in optics and acoustics are well understood, but the variation in acoustic impedance for sound/ultrasound is much higher than the variation of index of refraction for electromagnetic radiation. The standard anti-reflection method is to design an

interface layer that has the geometric mean (square root of the product) between the two indices/impedances. When this coating has a thickness of a quarter of a wavelength, the reflected waves from the two interfaces of the coating will be of equal magnitude and out of phase so reflected waves cannot propagate. The impedance mismatch between commercial 1-3 25% PZT ceramic composites and petroleum is only a factor of 7.5 with a geometric mean of 3.55. A conventional single layer quarter-wave anti-reflection coating of filled epoxy can easily match this and give good performance.

The disparate impedances of natural gas and lead zirconate titanate (PZT) ceramics or single crystals are approximately a factor of 3,000 different at 500 psi and difficult to match for the propagation of waves through the interface. Unless ameliorated by an impedance matching coating, this results in almost complete reflection as if one were trying to pass light through a mirror. A single geometric mean layer would require a material of Z = 0.6 MRayl, but a single impedance matching coating between such disparate impedances will be sharply tuned to a narrow wavelength range and therefore have extremely limited bandwidth only ~5%.

Higher performance, in both sensitivity and bandwidth is possible with two or more quarter-wave layers. Multiple quarter-wave layer coatings have been shown to improve transducer bandwidth and reduce ringing. The formula for such coatings is given by each layer being optimized by having an impedance that is the geometric mean between the materials on either side.

The fundamental problem remains how low an impedance may be achieved in the outermost layer. It will be seen that the 1 bar requirement of 0.01 MRayl in the outer layer is simply not possible for a functional material. In practice, the outermost layer is set by the best available material and the other layer(s) are tuned accordingly. While the increased gas impedance at high pressure reduces that mismatch, the material must be incompressible.

The solution developed in this project to impedance matching to air and gas improves on existing air-coupled coatings with transducer sensitivity four times that of legacy devices even before inclusion of single crystal PZT. All project milestones were completed.

Of course, there is no such impedance-matching coating on the inside of the steel pipe so the high losses there must be compensated with still better transducer performance.

Transducer characterization

The discussion below covers the final test results that prove the effectiveness of the transducer meeting the project objectives.

Gas-coupled Ultrasonic Thickness Measurement

To determine the effectiveness of the gas-coupled ultrasonic transducers developed herein for inspection of gas pipelines, experiments were performed in a pressurized gas environment to measure the thickness of carbon steel plates. Several of the 2 MHz gas-coupled transducers developed in this project were tested and the optimum transducer was selected to be used for thickness gauging using the pulse-echo technique. In this technique, a single gas-coupled ultrasonic transducer is used to transmit and receive the ultrasonic waves from the transducer into the pressurized gas, into the carbon steel plate and back to the transducer. Figure 20 shows the schematic drawing of this technique.

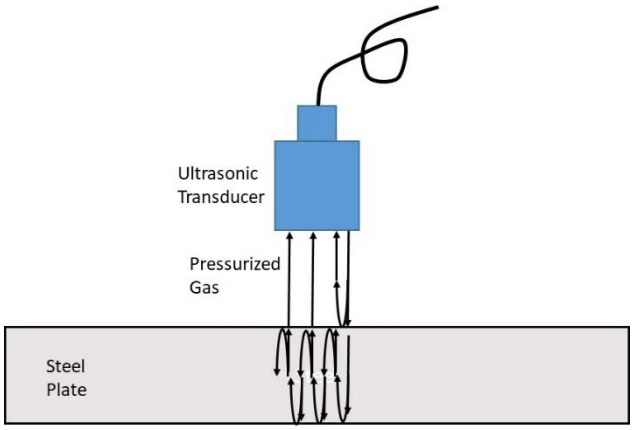

Figure 20. Schematic drawing of the pulse echo technique.

As the figure shows, the transmitted ultrasonic waves travel through the pressurized gas and intersect the top surface of the carbon steel plate. Owing to the large impedance difference between the pressurized gas and the carbon steel plate, most of the ultrasonic energy (more than 99.9%) is reflected back from the interface to the transducer and only a small portion of the energy enters the plate. The portion of the ultrasonic energy entering the plate travels toward the back surface of the plate and most of the energy is reflected back to the top surface of the plate (one case where the impedance mismatch is favorable). Again, most of the ultrasonic energy impinging on the top surface is reflected back at the top surface toward the bottom surface. The small portion of the ultrasonic energy that is transmitted through the top surface of the plate travels toward the transducer through the pressurized gas and can be detected by the GCUT now acting as a sensor in pulse-echo mode. In fact, the ultrasonic energy inside the carbon steel plate reverberates repeatedly between the top and back surfaces inside the plate and only a small portion of the energy is transmitted through the interface every time the ultrasound encounters it, so consecutive reflections are similar in magnitude. The reverberated ultrasonic energy that is transmitted through the top surface is detected by the original GCUT and can be displayed on an oscilloscope.

Figure 21 shows the amplitude of a typical signal received by a GCUT in pulse-echo mode versus time. As the figure shows, the first signal in the waveform is the reflected signal from the top surface of the steel plate. This signal is inherently approximately a factor of 1,000 stronger than the back-wall reflections, since most of the ultrasonic energy is reflected back from the top surface of the sample. This is determined by the impedances of the steel and the gas, the latter of which in turn is determined by the pressure. The subsequent signals in the waveform are the small amount of transmitted ultrasonic energy through the steel-gas interface each time from the reverberated waves inside the sample. These reverberated signals are ~60 dB smaller than the reflected signal from the top surface of the plate but consecutive signals are similar in magnitude so analyzing multiple higher order signals may be used to measure the sample thickness. The time between these reverberated signals is determined by the thickness of the plate and the speed of sound.

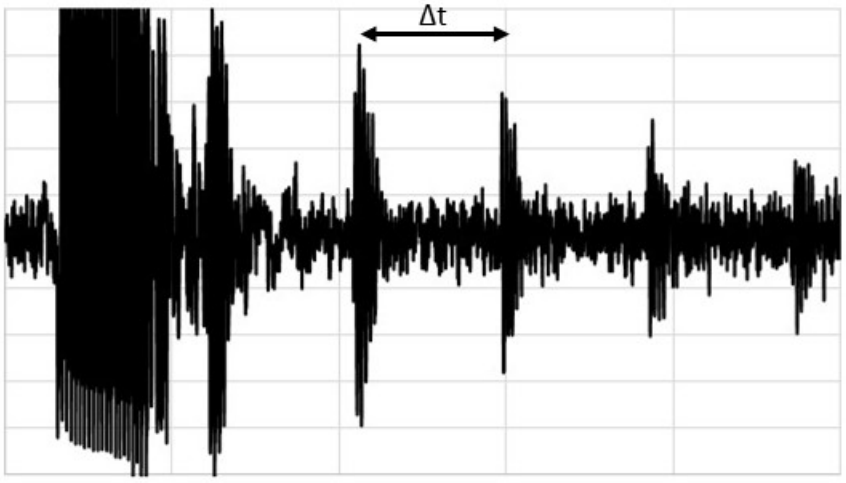

Figure 21. An A-scan waveform obtained over a 1-inch plate at 250 psi of nitrogen.

By measuring the time difference between these reverberated signals (*Δt*), one can determine the thickness of the plate. If the thickness of the plate is *D*, the formula to determine it is shown in Equation 1:

$$D = \frac{\Delta t \times v_s}{2} \qquad (1)$$

where v_s is the speed of sound in carbon steel.

Sample Preparation

To measure different thicknesses using this gas-coupled ultrasonic technique, a carbon steel sample plate was made with four different thicknesses. These thicknesses were machined as different size steps. Figure 22 shows a schematic drawing of the stepped carbon steel sample.

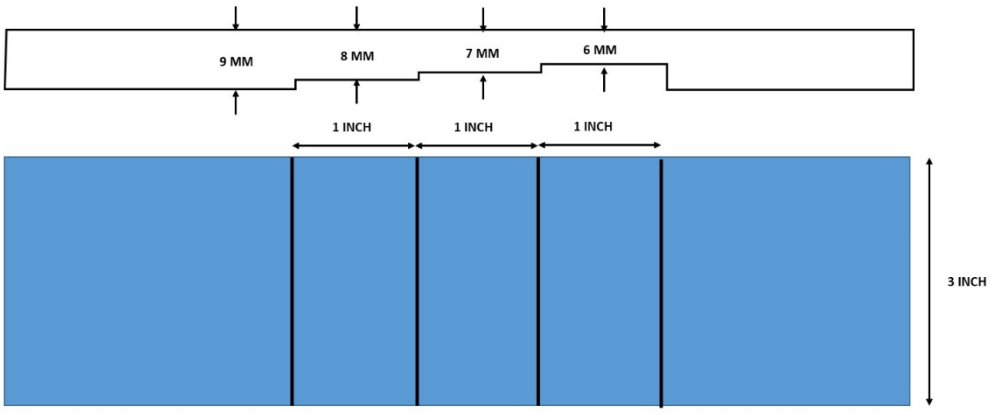

Figure 22. Schematic drawing of the step sample.

The step sizes shown above are nominal thicknesses and, after the steps were machined, the thickness of each step was measured using a micrometer. Figure 23 shows the sample that was used for thickness measurement. As the picture shows, the use of this sample enabled measurement of four different carbon steel thicknesses of about 9 mm, 8 mm, 7 mm and 6 mm.

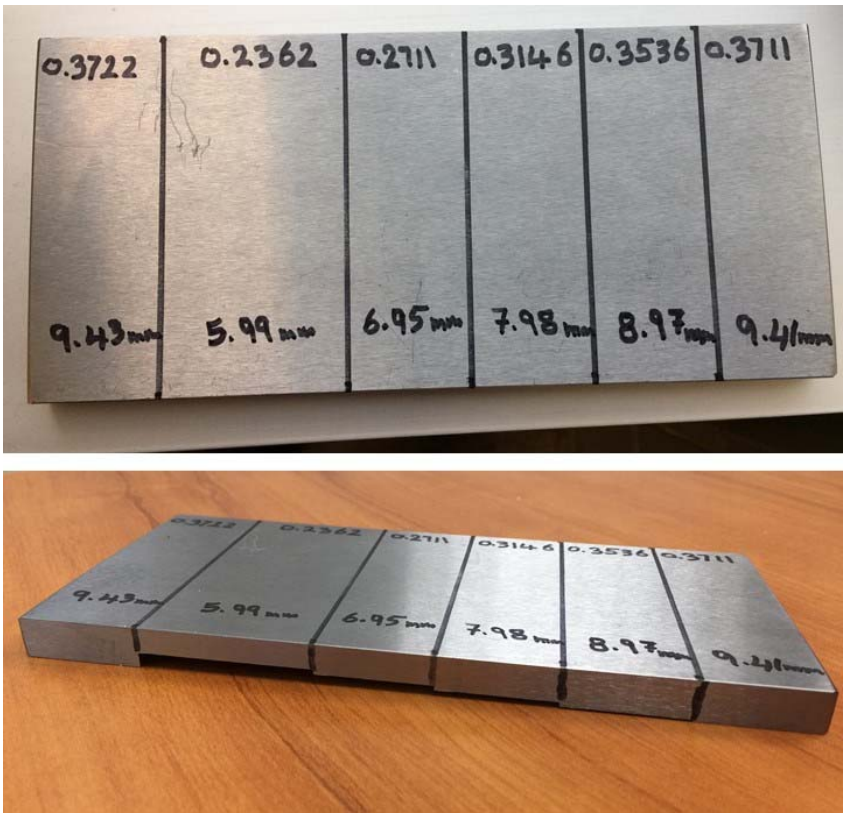

Figure 23. Carbon steel step sample used to measure different thicknesses.

Experimental Procedure

The stepped carbon steel sample was placed inside the pressure chamber on loan from GTI under the GCUT. The transducer manipulators inside the chamber are capable of rotating the transducer to be normal to the surface of the sample and translate the transducer to perform scanning of the transducer over the sample. Figure 24 shows the experimental setup used for gas-coupled ultrasonic thickness measurement. As the figure shows, the sample is placed under the transducer with a standoff of 25 mm, and the transducer is connected to a manipulator that can rotate and move the transducer over the sample.

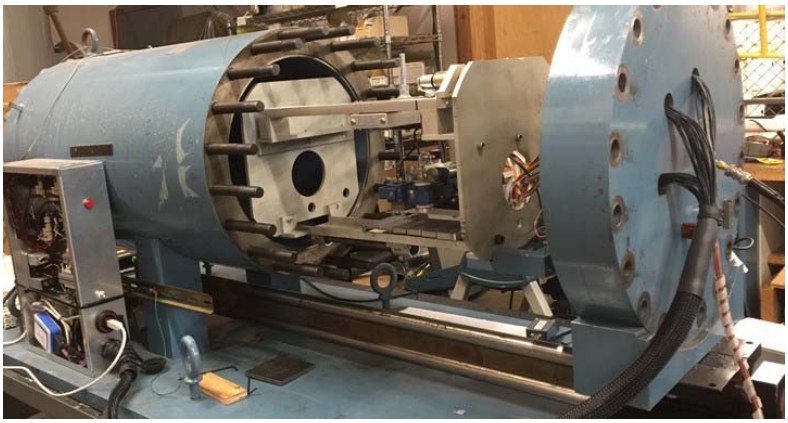

Figure 24. Experimental setup for gas-coupled ultrasonic thickness measurement.

After adjusting the transducer over the stepped sample, the chamber was closed and nitrogen was used to pressurize the chamber. Nitrogen has a slightly different impedance than natural gas, but otherwise behaves similarly and is obviously much safer to use. For this set of results, the chamber was pressurized to 250 psi (about 17 bars). This is a fairly low pressure compared to transmission line pressures, which are more than 1,000 psi. This pressure setting (250 psi) is comparable to low end pressures in distribution pipelines. As the pressure is increased, the performance of the transducer will improve so this test validates performance in the worst operational case. This low setting was chosen to demonstrate the effectiveness of this technique in low pressure distribution lines.

When the desired pressure was achieved, the transducer was placed over each step and the waveforms were recorded to measure the thickness of each step. Additionally, the transducer was scanned over the four steps and data were recorded and analyzed to generate continuous data collection and automated signal processing and thickness measurement. No averaging was required.

Results

First, the transducer was placed over the step with nominal thickness of 9 mm at a standoff of 25 mm. Then it was moved over the other steps with nominal thicknesses of 8 mm, 7 mm, and 6 mm. Figures 25 to 28 show the portions of the waveforms that contain multiple reverberated signals between the front and back surfaces of the sample. There is very little decay between the peaks as most of the ultrasound continues to be internally reflected. As the figures show, for each step size the time between the reverberations changes. The time between these echoes was used to calculate the exact thickness of each step. The speed of sound used to compute thicknesses using the gas-coupled ultrasonic technique was 5,900 m/s, which is a typical value used for the speed of sound in carbon steel. It should be noted that the transducer itself is so effective that the thickness can actually be determined to within a few percent simply by using the cursor on the oscilloscope screen to estimate the period with no signal processing or averaging.

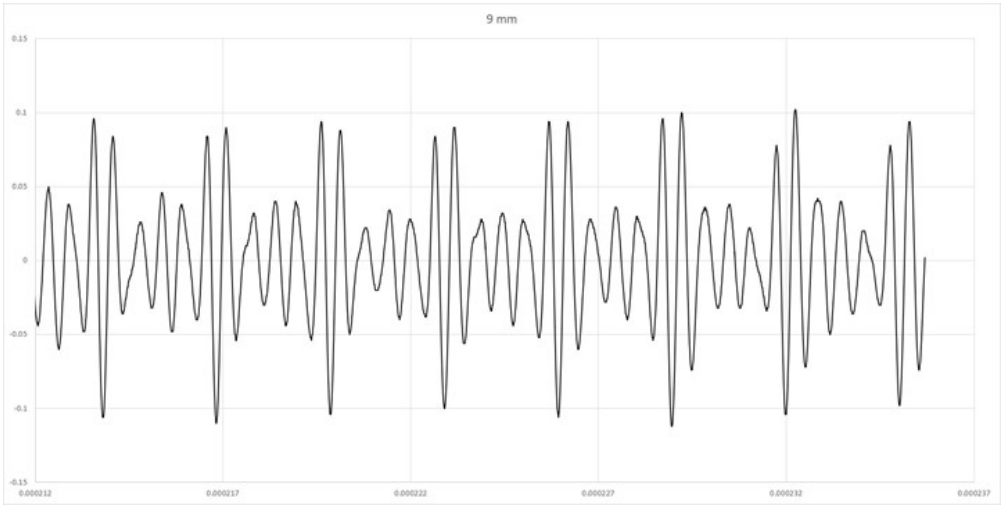

Figure 25. A-scan of gas-coupled UT over a 9 mm step.

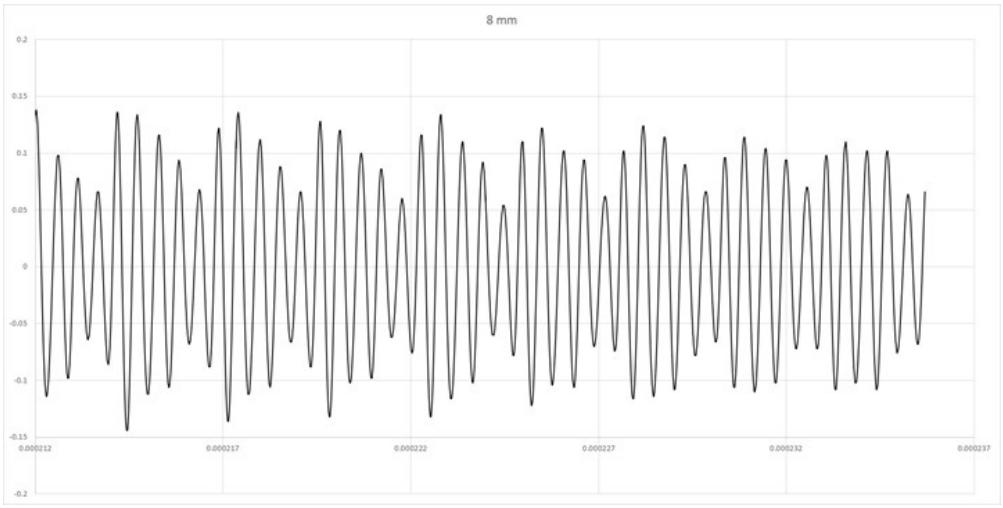

Figure 26. A-scan of gas-coupled UT over an 8 mm step.

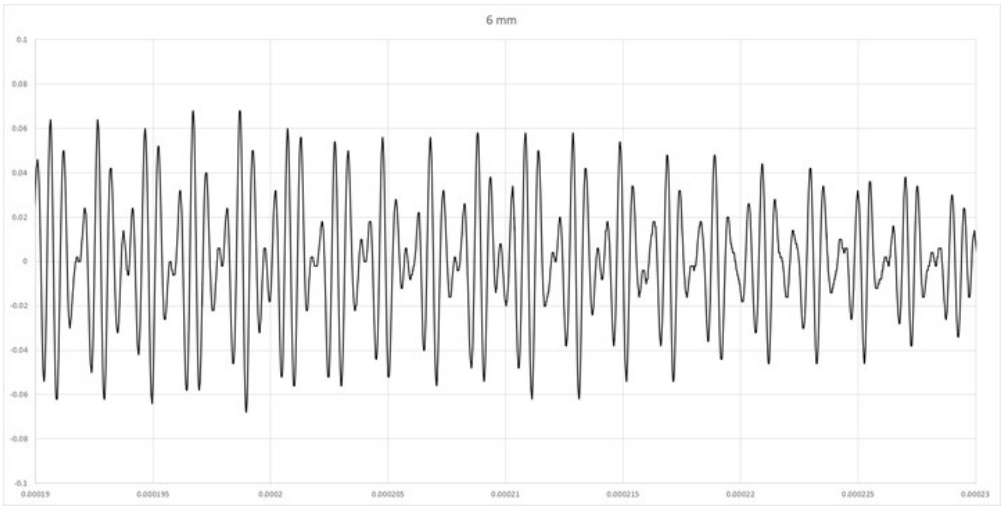

Figure 27. A-scan of gas-coupled UT over a 7 mm step.

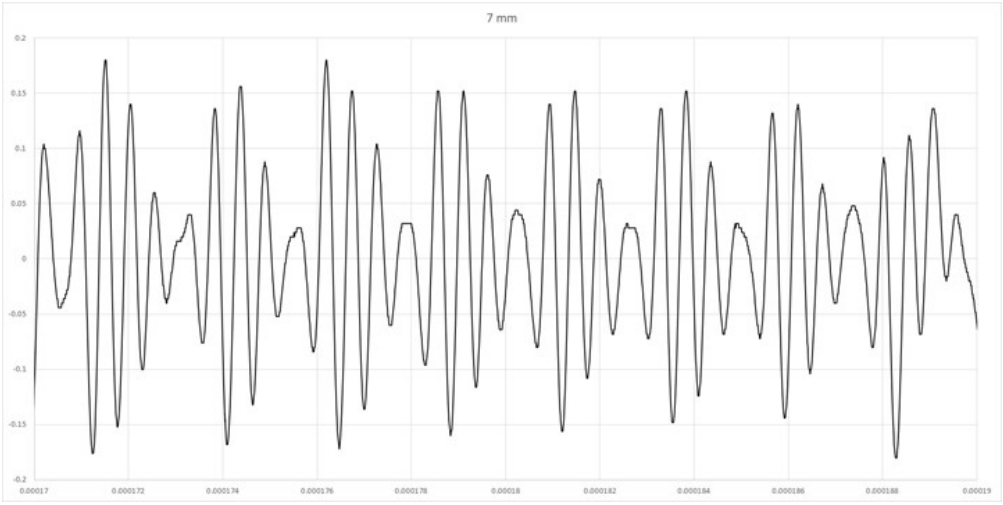

Figure 28. A-scan of gas-coupled UT over a 6 mm step.

An innovative signal processing procedure was developed to compute the time between the echoes (Δt) and calculate the thicknesses based on Equation #1. This procedure was used on the waveforms shown in Figures 25-28 and the thickness for each step was computed. Table V shows the computed thicknesses using the gas-coupled ultrasonic technique compared to micrometer measurements for all four steps.

Table V. Measured and computed thicknesses of the carbon steel step sample.

Nominal Thickness	**9 mm step**	**8 mm step**	**7 mm step**	**6 mm step**
Micrometer Measured Thickness	8.97 mm	7.98 mm	6.95 mm	5.99 mm
Gas-Coupled UT Measured Thickness	8.93 mm	7.97 mm	6.99 mm	5.96 mm

As the table above shows, the maximum difference between the micrometer measurement and the gas-coupled UT measurement is less than 0.05 mm. Typically, the error in ultrasonic thickness gauging is around 0.1 mm. We expect to have at worst the same error using this GCUT method. This uncertainty is below the target of 0.13 mm set in the specifications review above.

Finally, the gas-coupled transducer was scanned over all the four steps simulating data collection during an ILI run inside a pipe. The data were taken with 1 mm resolution, well below the specified target. However, when the transducer was between two thicknesses (over the step), the signal processing procedure is currently unable to measure the thicknesses. In these regions, the incident beam of the ultrasonic transducer generates echoes based on both thicknesses. Therefore, the time between echoes (Δt) becomes ambiguous. The extent of these regions depends on the size of the beam or diameter of the transducer. The gas-coupled transducer used in this experiment is about 10 mm diameter, thus the ambiguous region must be around 10 mm as well.

Figure 29 shows a schematic drawing of the scan area over the step sample. As can be seen, the scan was started from the middle of the 9 mm step and finished on the middle of the 6 mm step. Therefore, the scanned areas over these two steps are half of the other two steps. Figure 30 shows the results of this scan. As Figure 30 shows, no accurate thickness data were obtained when the transducer was located between the two surfaces (over the steps).

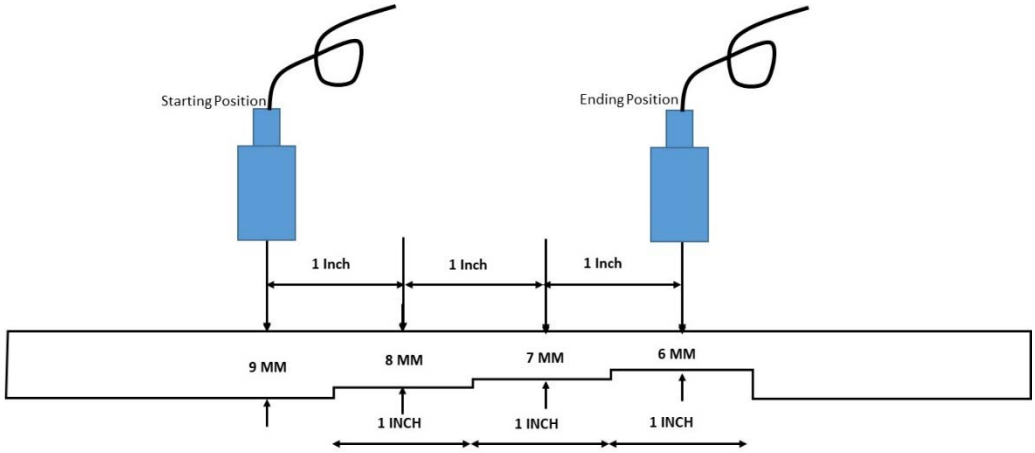

Figure 29. Schematic drawing of the scan area over the step sample.

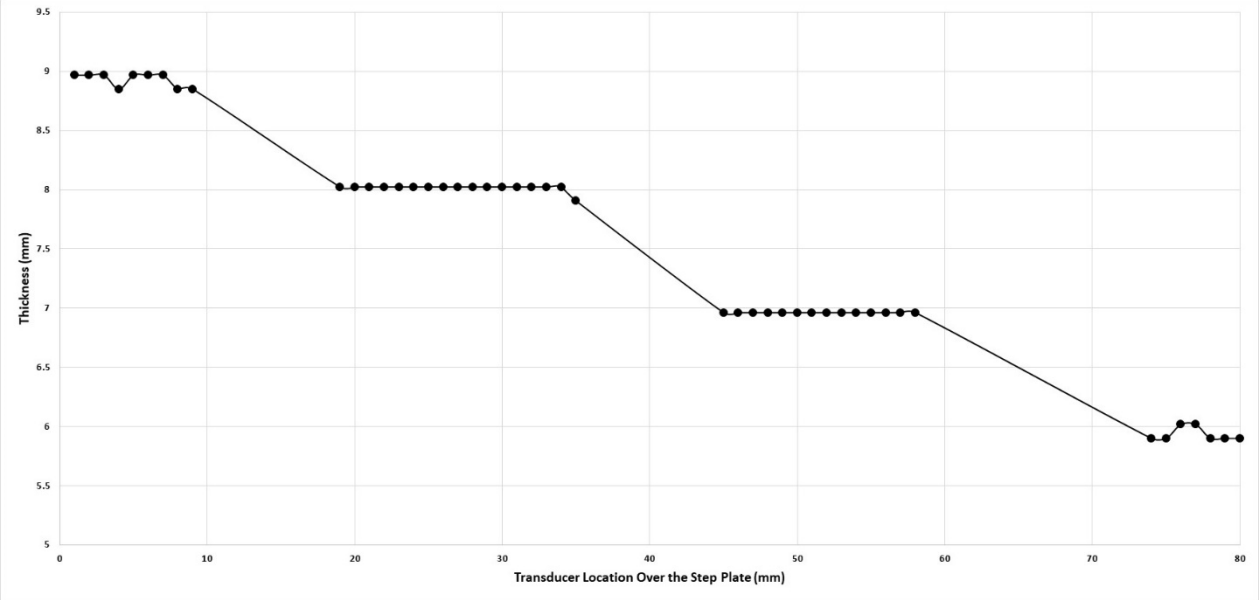

Figure 30. Result of the scan over all the four steps.

In future data processing, it is planned to resolve the ambiguity of the area between steps so multiple thicknesses can be measured as, for example, would be the case for a small pit or for a gradient in corrosion.

Development of an Ultrasonic Profilometry/Caliper ILI Tool for Gas Pipelines

Background

Pigging has become an integral part of any pipeline integrity program. Continuous and safe operation of a pipeline requires periodic cleaning and inspection to ensure defects do not grow beyond critical sizes to compromise the integrity of the pipeline and cause sudden release of products. Although both liquid and gas pipelines are susceptible to critical damage, gas pipelines could pose more danger since pressurized gas possesses more energy as it can expand rapidly if a failure occurs and natural gas is more explosive than, for example, crude oil. Gas pipeline operators are concerned about such failures and perform regular examinations of their pipelines using ILI tools (pigging).

Performing inspection of pipelines using smart pigs (currently typically MFL) requires preparation to avoid any incident during the ILI runs. Any obstruction in the pipeline could trap the pig inside the pipe and disrupt the operation of the line. The removal of a trapped pig in a pipeline can be a very tedious undertaking, since its location in the pipe is mostly unknown and the pipes are buried. In many cases, the ILI tool may need to be destroyed to restart the operation of the pipe. The cost associated with trapped pigs can be very high. This high cost stems from the disruption of operation of the pipeline and removal of the pig from the line.

Some gas pipelines are known to have obstructions that render them unpiggable, but all others must be examined to determine their status. To avoid scenarios of trapped pigs in a pipeline, operators perform a caliper run to obtain some information about the internal geometry of the pipe. The caliper (geometry) pigs can determine several features of the internal surface of the

pipe. The most important information that caliper pigs provide is Third Party Damage, usually caused by people and equipment working around the pipe and unintentionally damaging it. Damage can also occur during any repair to the pipe. This damage is mostly denting or deformation of the pipe that changes the roundness of the pipe.

The other important information that caliper pigs provide is the ovality of the pipe at different locations. Sometimes pipes lose their roundness due to external forces and their cross-section changes from a circle to on oval. This condition can cause some inspection pigs to get trapped inside the pipe during the inspection runs. Additionally, caliper pigs can find any accumulation of product residues that can obstruct the passage of the inspection pigs.

Caliper pigs can also find any misalignment of the pipes at girth welds or excessive weld root that could obstruct the passage of the inspection pig. Other information that caliper pigs can provide includes the presence or condition of the valves, attachments that have intruded into the pipe or any internal modification of the pipe. Caliper pigs are also used after commissioning of new pipelines or after any repair or modification of the line.

To summarize, caliper pigs are used to measure the inside geometry of the pipelines. They are essential before performing ILI inspection runs with surface-riding tools to determine the condition of the pipeline. They are used to characterize:

1) Surface condition, residues
2) Internal corrosion, pit depth and dimensions,
3) Valves, fittings, excess weld root,
4) Ovalities,
5) Dents, hidden third party damage,
6) Misalignment,
7) Internal pipeline diameter and passage clearance for surface-riding ILI tools such as Magnetic Flus Leakage (MFL).

Limitations of Caliper Pigs

Although caliper pigs can provide a lot of valuable information about the internal condition of the pipe, current tools are very low resolution. Most of the caliper tools use mechanical fingers that touch the internal surface of the pipe and the tool detects any perturbation of the fingers as they travel along the pipe (Figure 31). There are also some caliper ILI tools that use electromagnetic sensors to detect any changes in the internal surface of the pipe.

Figure 31. Conventional caliper pig with "fingers."

The number of mechanical fingers or sensors are limited in current caliper pigs and provide a poor resolution of the surface geometry of the pipe. It would be

advantageous to have a high-resolution caliper tool that could perform detailed surface profilometry of the internal surface of the pipe. High-resolution surface profilometry would be able to find more accurately all the information that a caliper tool provides. In addition, a high-resolution caliper can detect and profile any internal corrosion in the pipe. Such a high-resolution description of the internal corrosion in gas pipelines could be better than the current description of internal corrosion performed by Magnetic Flux Leakage (MFL) tools. Additionally, a tool that can perform with significant standoff can detect all these types of conditions without risk of being trapped itself and can operate in currently unpiggable pipelines.

Proposed Ultrasonic Profilometry/Caliper ILI tool for Gas Pipes

Generally, ultrasound has high accuracy and resolution to describe the surface features of a pipe. However, in a gas environment ultrasound cannot couple and propagate efficiently. This limitation has prevented developers from using ultrasound for condition assessment of the internal condition of pipelines.

Current advances in development of efficient gas-coupled ultrasonic transducers in this project, have provided an opportunity to examine the feasibility of using ultrasound to perform surface profilometry. These new GCUTs have been shown to be capable of generating and receiving strong signals through the gas from the front surface of a carbon steel sample to determine accurately the distance of the front surface from the ultrasonic transducer. By receiving reflected ultrasonic signals from the internal surface of a pipe, one can reconstruct the features of the internal surface. An ultrasonic profilometry/caliper pig could detect corrosion, ovality and roundness problems, dents and other damage by third parties, pipe misalignment and girth weld intrusion, valves and other geometrical changes to piggable and unpiggable pipes. All these features could be detected with high accuracy and resolution with ultrasound.

Feasibility Experiments

To investigate the feasibility of using ultrasound for internal surface profilometry of pipelines, several experiments were performed. These experiments included scanning GCUTs over a carbon steel sample in a pressurized gas chamber. Different features were machined into the carbon steel sample to simulate typical features in the internal surface of a pipe. The chamber was pressurized with nitrogen gas and the pressure of the gas was held at 200 psi during the scan. Higher gas pressures are more common in gas pipelines and greatly benefit ultrasonic propagation in gas and examination of surfaces, but 200 psi was chosen to show even low-pressure pipes can be inspected by such ultrasonic ILI tools.

In the first experiment, a carbon steel plate of 8”x8”x0.5” was used. Several different sized flat bottom holes (FBH) with different depths were machined into the sample. Figure 32 shows a schematic drawing of Plate #1 with different sized FBH.

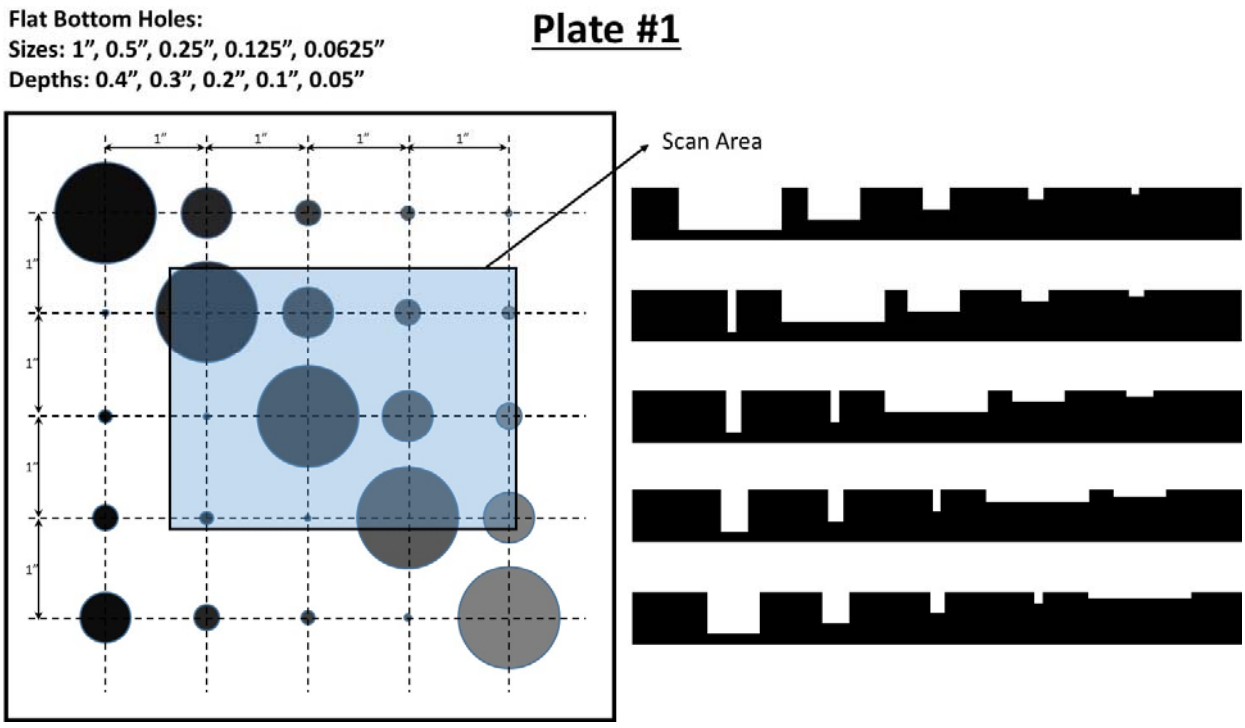

Figure 32. Schematic drawings of plate #1 with machined flat bottom holes to simulate corrosion.

The scanner inside the pressure chamber has a limited scanning area. Furthermore, the scanning area of the pressure chamber is located off-center from where the sample sits. Figure 32 also shows the location of the scanning area for this experiment.

In this experiment, a 1.5 MHz gas-coupled ultrasonic transducer was placed 1" above the sample and it was scanned over an area of 60 mm × 80 mm (~2.4" × 3.15"). The resolution for this scan was 1 mm. Figures 33 and 34 show the results for this scan.

The planar dimensional units in Figures 33 and 34 are millimeters. Figure 34 also shows the depth of the flat bottom holes in millimeters. These figures show that most of the FBH's were detected in this experiment. The 1-inch diameter holes are clearly detected and their depth measured fairly accurately. The 0.5-inch and 0.25-inch FBH's were also detected. The smallest FBH in this scan area was 0.125-inch, and it was located on the upper right side at the border of the scan area. The results in Figure 33 and 34 show some indication of this small size FBH in these images.

To analyze the results in more detail, 2D plots of depth variation along both scan directions are shown in Figure 35. The locations of scanned lines AA, BB, CC and DD are shown in Figure 33.

Figure 35 shows the ultrasonically measured depth of the holes along line AA is about 7.5 mm for 1" diameter FBH, 4.9 mm for 0.5" diameter FBH and 2.1 mm for 0.25" diameter FBH. The actual depths of these holes are 7.6 mm, 5.1 mm and 2.5 mm respectively. The ultrasonic transducer (UT) measured depths of the holes along line BB are about 4.9 mm for 1" diameter FBH and 2.3 mm for 0.5" diameter FBH. The actual depths of the holes along line BB are 5.1 mm and 2.5 mm respectively.

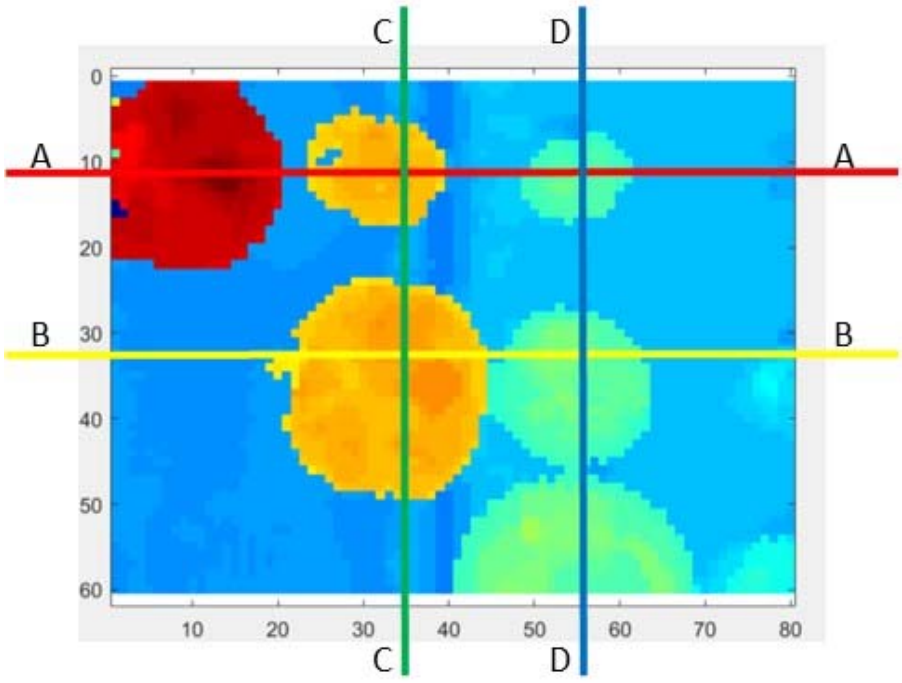

Figure 33. C-scan of ultrasonic profilometry over Plate #1.

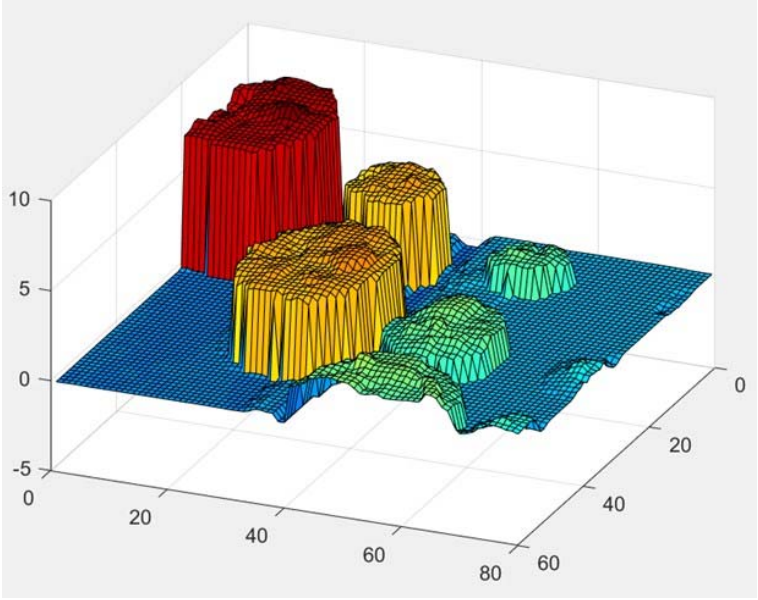

Figure 34. 3D surface plot of ultrasonic profilometry over Plate #1.

Figure 35 shows the UT measured depths of the holes along line CC are 5 mm and the actual depths are 5.1 mm. Finally, the UT measured depths of holes along line DD in Figure 35 are about 2.3 mm, and the actual depths are 2.5 mm. Thus, these scans show the depths of FBH's could be measured within a few tenths of a millimeter.

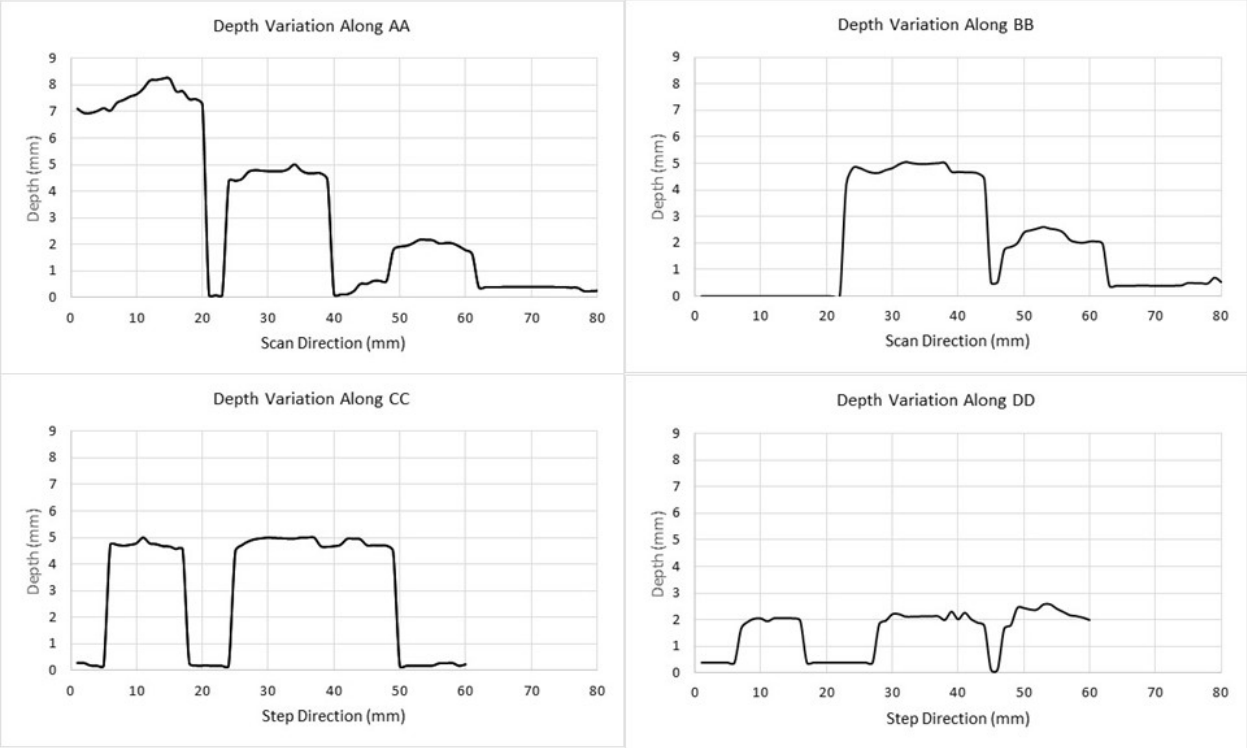

Figure 35. Depth variation along scan and step directions.

Minimal filtering and signal processing were used on these results. More accurate measurements could be achieved if the signals were filtered more rigorously and more signal processing was applied to the results.

Plate #1 had only flat bottom holes machined into it. To test a more realistic simulation of corrosion, another carbon steel plate with round bottom holes was used. Plate #3 has different sized round bottom holes, holes in holes and some holes in cavities to simulate a more realistic corrosion surface. Figure 36 shows a schematic drawing of this plate including the scan area.

The sample was placed in the pressure chamber under 200 psi pressure of nitrogen gas. A 1.5 MHz gas-coupled ultrasonic transducer was scanned over the sample and the results were recorded. The C-scan of the data is shown in Figure 37. To show the depth variation better, a 3D surface plot of the analyzed data is shown in Figure 38. As Figures 37 and 38 show, most of the round holes and cavities have been detected. However, two of the 0.25-inch round holes that are separated by only 0.0625 inch do not show as two separate holes. Due to the size of the ultrasonic beam, such close holes may not be distinguished as separate features. These limitations can be further determined with more samples and experiments. There is sufficient back-reflected intensity that it is anticipated smaller diameter transducers with better resolution will be possible.

Again, to analyze the ultrasonic depth determination of the holes further, 2D plots of depth variation along both scan directions are shown in Figure 39. The scanned lines EE, FF, GG and HH are shown in Figure 37. Figure 39 shows the UT measured depths of the two cavities along the line FF are about 3 mm and 6 mm. The actual depths of these cavities are 3.2 mm and 6.3 mm

respectively. The UT measured depths of the holes inside these cavities along the same line (FF) are measured ultrasonically as 7 mm and 10 mm. The actual depths of these holes are 6.3 mm and 9.5 mm.

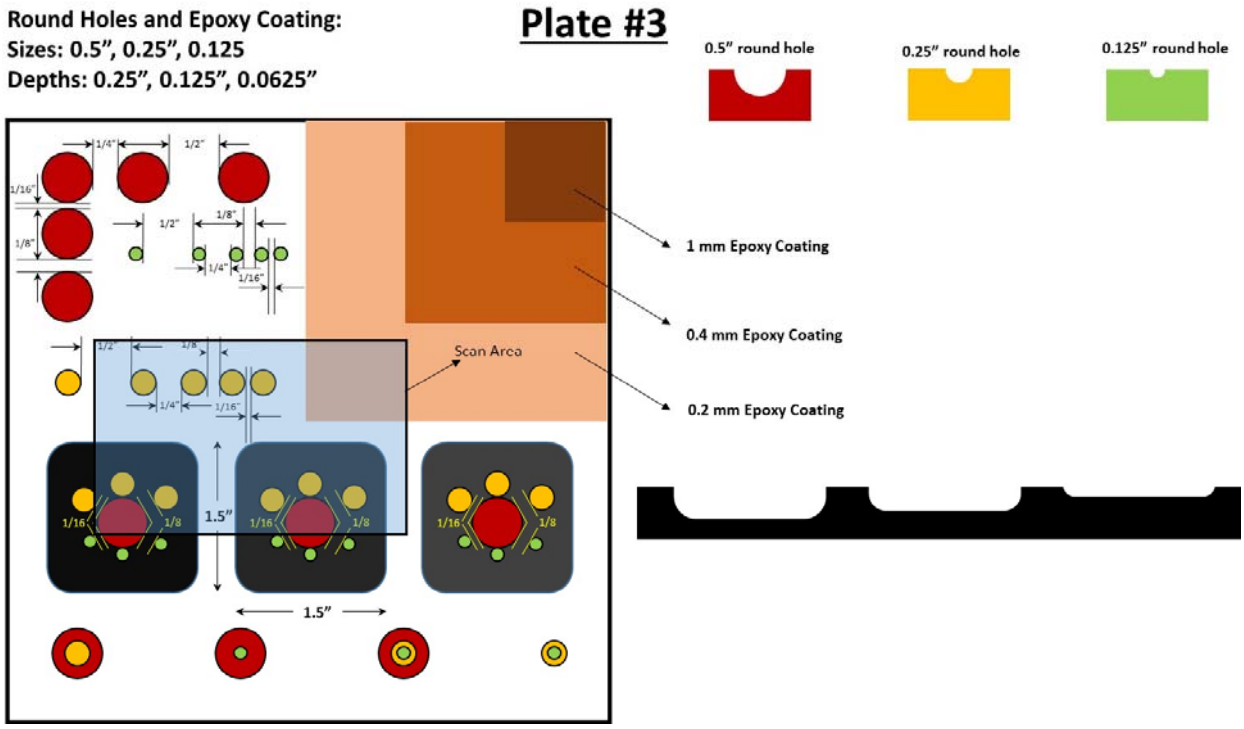

Figure 36. Schematic drawing of Plate #3 with different sized round holes.

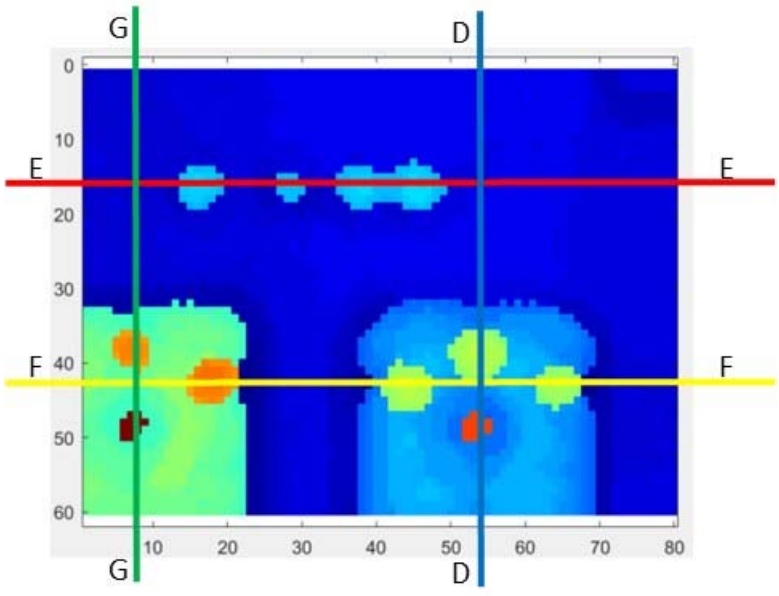

Figure 37. C-scan of ultrasonic profilometry over Plate #3.

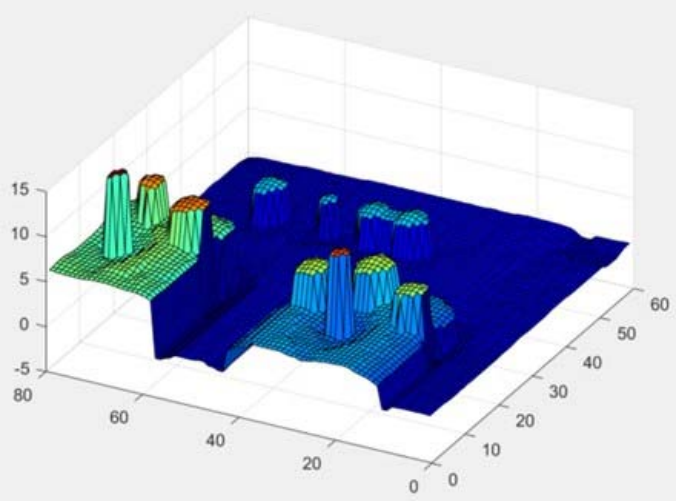

Figure 38. 3D surface plot of ultrasonic profilometry over Plate #3.

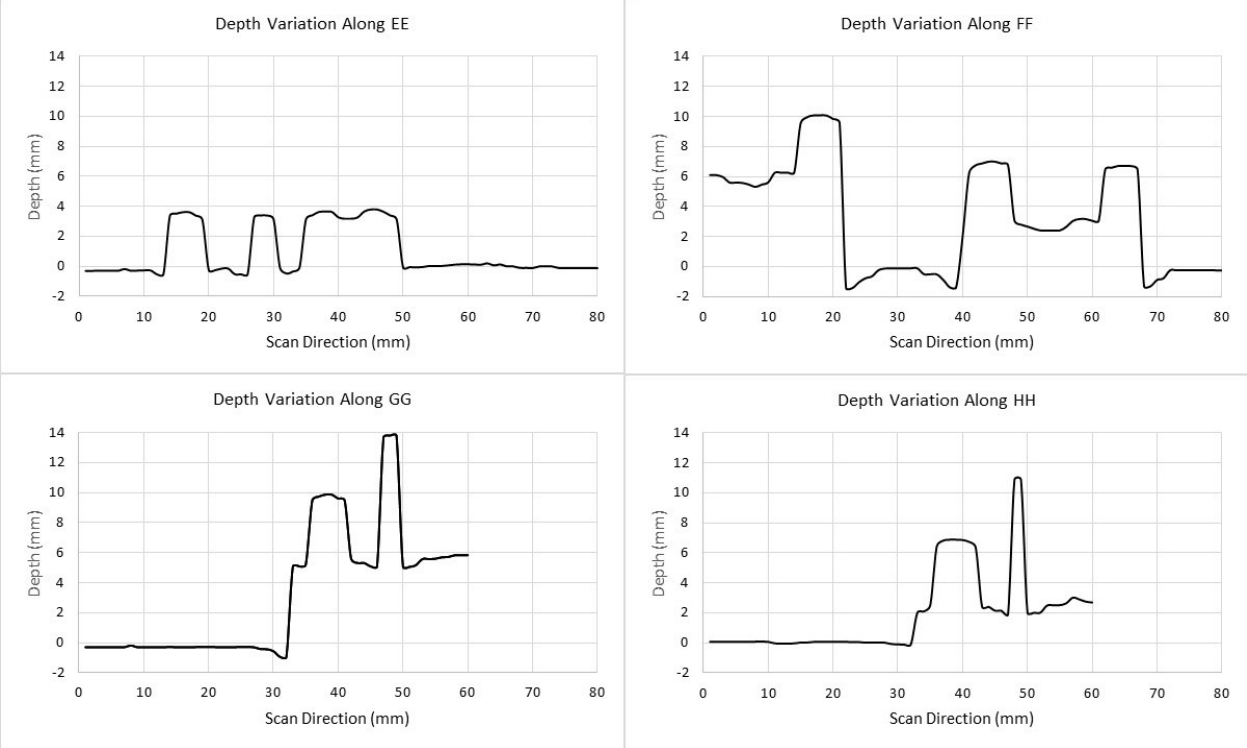

Figure 39. Depth variation along scan and step directions.

Figure 39 shows the depth of the holes along line EE. As mentioned before, two of the holes that are very close together (0.0625 inch) are detected as one hole. However, the figure shows the UT measured depths of these holes are about 3.8 mm. The actual depth of these holes is 3.2 mm.

The line GG in Figure 39 shows the UT measured depth of the cavity as 5.5-6 mm. The actual depth of the cavity is 6.3 mm. The depths of the holes along the line GG are measured ultrasonically to be 10 mm and 14 mm. However, the actual depths of these holes are 9.5 mm and 12.5 mm.

Finally, the plot in Figure 39 shows the UT measured depth of the cavity as about 2 mm and the depths of two holes as about 7 mm and 11 mm along the line HH. The actual depth of the cavity along the line HH is 3.1 mm and the depths of the two holes are 6.3 mm and 9.5 mm.

Observation of Dents and Pits

The measurements taken below were done at the behest of Qi2's commercialization partner, Q-Inline, to show the immediate capability of a potential tool. The left side of Figure 40 shows a new test sample made up including wide area machined regions simulating general corrosion, holes inside and outside those areas to show pits and embedded protruding features including a ball bearing and screw heads. The plots on the right side of Figure 40 show a 3D and planar visualization, with very accurate measurements in the latter.

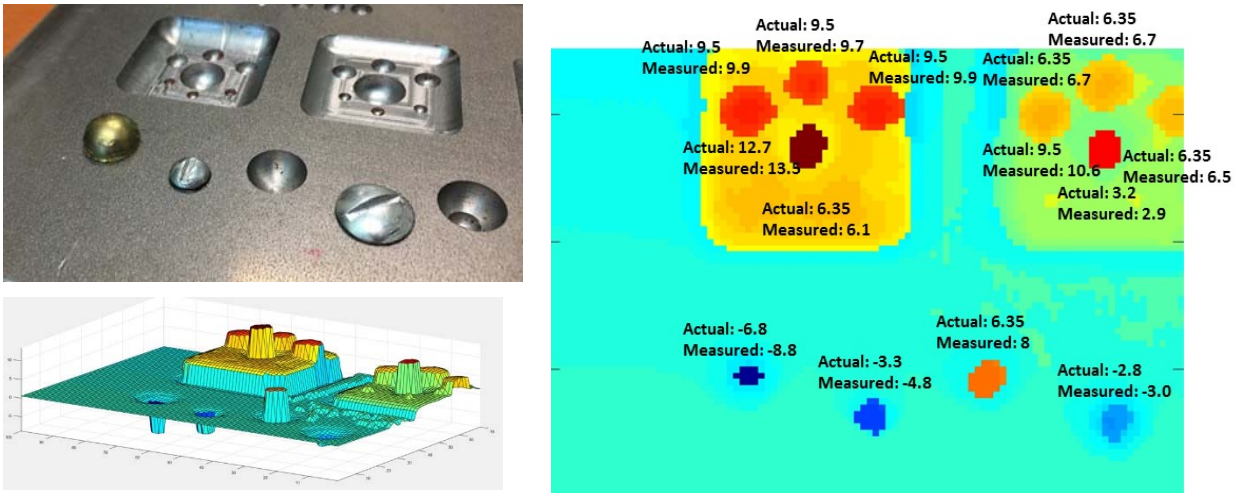

Figure 40: High resolution depth measurement (positive numbers) of round bottom machined holes (including holes in a machined section) simulating corrosion, and height measurement (negative) of screws and a ball bearing simulating protruding defect.

The customer also requested data on simulated dents from, for example, third party damage. These simulated dents were 3D printed according to customer specifications and include vertical sidewalls in some cases. The transducer was able to image them accurately from a perpendicular orientation, even including the vertical sidewalls. The dimensional measurements were highly accurate as can be seen from Figure 41.

As these preliminary results show, the accuracy of the depth measurement using gas coupled ultrasonics is a few tenths of a millimeter using only a single front surface reflection and minimal signal processing. Although further experiments and signal processing are required to identify the capabilities and limitations of this technique, the measurements already seen far surpass the capabilities and limitations of current caliper pigs.

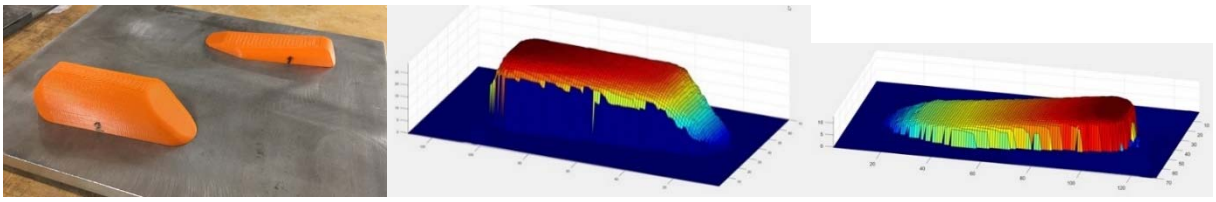

Dent	Width		Length		Height	
	Actual	Meas.	Actual	Meas.	Actual	Meas.
#1	34 mm	37 mm	100 mm	99 mm	6-12.8 mm	6.34-12.9 mm
#2	34 mm	38 mm	101 mm	95 mm	24.2-28.7 mm	23-29 mm

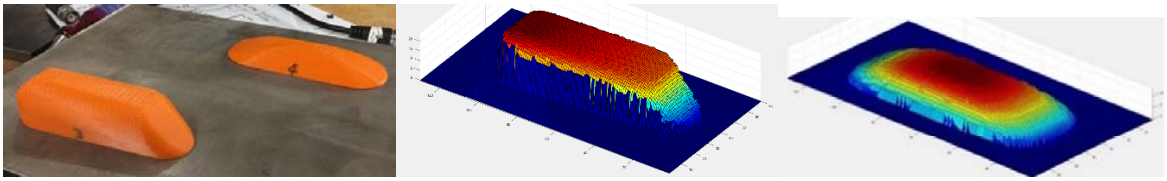

Dent	Width		Length		Height	
	Actual	Meas.	Actual	Meas.	Actual	Meas.
#3	34 mm	38 mm	100.5 mm	98 mm	19-24 mm	18.3-24.2 mm
#4	38 mm	39 mm	100 mm	101 mm	12.96 mm	13.01 mm

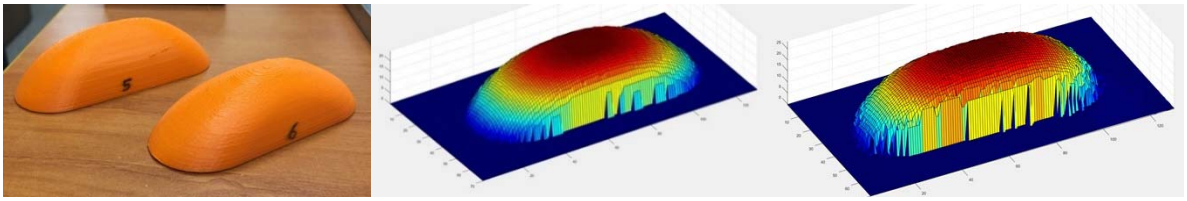

Dent	Width		Length		Height	
	Actual	Meas.	Actual	Meas.	Actual	Meas.
#5	38 mm	35 mm	101 mm	101 mm	28.36 mm	28.41 mm
#6	38 mm	39 mm	101 mm	103 mm	24.35 mm	24.44 mm

Figure 41: Profiles of simulated dents with accurate measurements.

Reporting

All reports for this contract are complete including this public version of the final report. The following conference technical presentations have been given:

- "[001] Lead Zirconate Titanate (PZT) Crystals with Composition Near the Morphotropic Phase Boundary," W. Zhu, V. Kovacova, V. J. Fratello, and S. Trolier-McKinstry, 2019

International Workshop on Acoustic Transduction Materials and Devices (IWATMD-2019) Penn State University, May 7-9, 2019.

- "Congruently Melting Perovskite Solid Solutions." Vincent Fratello, Lynn Boatner, Hanna Dabkowska, Antoni Dabkowski, Theo Siegrist, Christo Guguschev, Detlef Klimm, Darrell Schlom, and Shanthi Subramanian, International Conference on Crystal Growth and Epitaxy (ICCGE-19), Keystone, Colorado, August 1, 2019.

Intellectual Property

- Patent applications for the innovation of PZT liquid phase epitaxy "Method of Growth of Lead Zirconate Titanate Single Crystals" were filed in the United States, Japan, China and the European Union. The initial international patent cooperation treaty (PCT) application was published as WO 2014/130119 A2 and was favorably reviewed. The U. S. Patent 9,738,990 "Method of Growth of Lead Zirconate Titanate Single Crystals," inventor V. J. Fratello, was issued August 22, 2017. The equivalent Chinese patent ZL201380067374.9 was issued June 22, 2018. Notice of formal allowance was received from the Japanese Patent Office in December, 2018 and all fees have been paid. A divisional application has been filed to pursue additional claims in Japan. Negotiations are ongoing in the European Union.
- A Patent Cooperation Treaty (PCT) patent application for the substrate innovation entitled "Single-Crystal Perovskite Solid Solutions with Indifferent Points for Epitaxial Growth of Single Crystals" WO 2018/081809 A1 was filed October 31, 2017. This received a completely favorable PCT report from a U.S. based examiner. U. S. Patent 10,378,123 B2 was issued January 3, 2019 including the main claims and the other claims have been filed as a continuation. Applications were filed in April 2019 in Europe, China and Japan. Florida State University and IKZ Berlin have grown initial crystals as discussed herein.

Commercialization

Q-Inline (Quanta Inline Devices, Inc.), a high-growth US inline pipeline inspection company, and Qi2 announced details of their new technology alliance at the 2018 International Pipeline Exposition starting with new generation EMAT inline technology to improve inspection of smaller diameter pipelines.[15]

Q-Inline serves customers in North and South America, Europe and the Asia Pacific. They are headquartered in Houston, with offices in Michigan and Singapore, Q-Inline is a company of Quanta Services (NYSE: PWR), a Fortune 300 electric power and pipeline services company.

The next tool conceived for this partnership is the internal geometry/caliper tool described above using specially developed gas-coupled transducers from this project. A test of this capability was successfully completed for Q-Inline.

The following tool will be a wall thickness ILI tool using sensors and electronics as described in the testing results of this report. The tests of this capability described above were successfully completed for Q-Inline in December 2019.

Qi2 plans to seek additional funding for implementation of these gas-coupled ultrasonic transducer (GCUT) and system innovations in inline inspection tools for internal geometry and

wall thickness measurements in unpiggable gas pipelines to be commercialized by Q-Inline. Tools for various diameter distribution and transmission lines at various pressures are anticipated.

References

[1] Y. Xie, "Synthesis and Characterization of Piezo-/ferroelectric Lead Zirconate-Titanate (PZT) Single Crystals and Related Ternary Ceramics," Ph.D. thesis, Simon Fraser University, 2013.

[2] Z.-G. Ye, A.A. Bokov, Y. Xie, and X. Long, 2013 International Workshop on Acoustic Transduction Materials and Devices, May 6-10, 2013—Penn State University.

[3] International Centre for Powder Diffraction Data, Powder Diffraction File PDF-2, Release 2014, Newtown, PA.

[4] Brian Julius and Ronald Staut, "From Powder to Parts: An Introduction to Manufacturing Piezoelectric PZT Ceramic Components." http://www.ceramicindustry.com/articles/95168-from-powder-to-parts-an-introduction-to-manufacturing-piezoelectric-pzt-ceramic-components American Piezoelectric Corporation.

[5] D. G. Schlom, L.-Q. Chen, C. J. Fennie, V. Gopalan, D. A. Muller, X. Pan, R. Ramesh and R. Uecker "Elastic Strain Engineering of Ferroic Oxides," MRS Bulletin **39** (2014) 118.

[6] L. W. Martin and D. G. Schlom, "Advanced Synthesis Techniques and Routes to New Single-Phase Multiferroics," Current Opinion in Solid State and Materials Science **16** (2012) 199.

[7] V. J. Fratello, L. Boatner, H. Dabkowska, A. Dabkowski, T. Siegrist, C. Guguschev, D. Klimm, D. Schlom, and S. Subramanian "Congruently Melting Perovskite Solid Solutions," International Conference on Crystal Growth and Epitaxy, Keystone, Colorado, August 1, 2019.

[8] V. J. Fratello "Single-Crystal Perovskite Solid Solutions with Indifferent Points for Epitaxial Growth of Single Crystals" U. S. Patent 10,378,123 B2 January 3, 2019.

[9] S. Trolier-Mckinstry, private communication, September 15, 2019.

[10] B. Jaffe, W. R. Cook and H. Jaffe, *Piezoelectric Ceramics*, Academic Press, New York, 1971

[11] Y. Cao, G. Sheng, J. X. Zhang, S. Choudhury, Y. L. Li, C. A. Randall and L. Q. Chen, "Piezoelectric Response of Single-Crystal $PbZr_{1-x}Ti_xO_3$ Near Morphotropic Phase Boundary Predicted by Phase Field Simulation," Appl. Phys. Lett. **97** (2010) 252904.

[12] C. A. Randall, N. Kim, J.-P. Kucera, W. Cao and T. R. Shrout, "Intrinsic and Extrinsic Size Effects in Fine-Grained Morphotropic-Phase-Boundary Lead Zirconate Titanate Ceramics," J. Am. Ceram. Soc. **81** (1998) 677.

[13] APC International, "Physical and Piezoelectric Properties of APC Crystals," Rev. 4, https://www.americanpiezo.com/apc-materials/piezoelectric-properties.html, Updated Jan. 2019.

[14] E. Blomme, D. Bulcaen and F. Declercq, "Air coupled ultrasonic NDE: experiments in the range 750 kHz to 2 MHz," NDT&E International **35** (2002) 417.

[15] Oil and Gas Technology, http://www.oilandgastechnology.net/news/q-inline-forms-strategic-alliance-qi2-deliver-new-generation-emat-inline-technology-improve September 28, 2018.